

5662-4543  
2  
2nd

**LIBRARY**  
**Michigan State**  
**University**

This is to certify that the  
thesis entitled

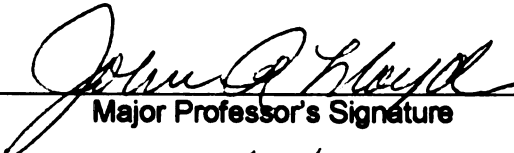
**NEW SURFACES FOR THE CONTROL OF BOILING HEAT  
TRANSFER: SITE FORMATION AT INCIPIENCE**

presented by

**NICOLE L. AITCHESON**

has been accepted towards fulfillment  
of the requirements for the

ME degree in MECHANICAL ENGINEERING

  
Major Professor's Signature  
8/15/03

Date

**PLACE IN RETURN BOX** to remove this checkout from your record.  
**TO AVOID FINES** return on or before date due.  
**MAY BE RECALLED** with earlier due date if requested.

DATE DUE	DATE DUE	DATE DUE

**NEW SURFACES FOR THE CONTROL OF BOILING HEAT TRANSFER: SITE  
FORMATION AT INCIPIENCE**

**By**

**Nicole Lea Aitcheson**

**A THESIS**

**Submitted to  
Michigan State University  
In partial fulfillment of the requirements  
For the degree of**

**MASTER OF SCIENCE**

**Department of Mechanical Engineering**

**2003**



## **ABSTRACT**

### **NEW SURFACES FOR THE CONTROL OF BOILING HEAT TRANSFER: SITE FORMATION AT INCIPIENCE**

**By**

**Nicole Lea Aitcheson**

Mircro-scale structured copper surfaces with periodic surface structure variations were successfully created using electrochemical deposition on inclined flat surfaces. The surface inclination angle has previously been shown to produce longitudinal vortices as the flow transitions from laminar to turbulent. Thus the surface structures created by the deposition process are a function of the surface inclination angle. The structure of these specially created surfaces was meticulously characterized using an Environmental Scanning Electron Microscope and an Atomic Force Microscope. Boiling incipience on the deposition surfaces of 15° and 30° was investigated and compared to that of a smooth reference surface. Boiling evaluation of the smooth, 15°, and 30° surfaces suggests that the more pronounced structure of the 30° surface increases the nucleation site density at boiling inception as compared to the other surfaces. These preferred nucleation sites at incipience formed by vapor trapping pockets and basins created by column-like protrusions on the deposition surface.

## **ACKNOWLEDGEMENTS**

I would like to express my sincere gratitude to my advisor, Dr. John R. Lloyd, for providing me with a superior education throughout my academic development. His support and guidance in the completion of this thesis has lead to skills and knowledge that extends well beyond books and theory. I thank my committee members Dr. D. Grummon and Dr. I. Wichman for their support of this thesis. To the Department of Mechanical Engineering, specifically the department support staff, I express my genuine appreciation for their devoted assistance.

I would like to recognize CRDF Grant # RPI-2337 and NSF Grant # HER-0090582 for financial support, without which the completion of this thesis would not have been possible. I sincerely thank Per Askland for the countless hours he spent helping me with the ESEM. To Ewa Danielewicz I extend the same gratitude for her assistance with the AFM whenever I needed it. I am grateful for the technical inspiration of Al Lawrenze whose input was invaluable to the completion of this thesis. I would also like to thank Lisa Ngai for her experimental support.

I am truly grateful to Dan Fickes for his limitless support and understanding during the completion of this thesis. Finally, I thank my parents, Nancy and Scott Aitcheson for teaching me how to work hard and never give up.

## TABLE OF CONTENTS

LIST OF FIGURES.....	v
LIST OF TABLES.....	vii
LIST OF APPENDICES.....	viii
NOMENCLATURE.....	ix
<b>CHAPTER</b>	
<b>1.0 Introduction.....</b>	<b>1</b>
1.1. Pool Boiling.....	2
1.2. Inception of Boiling.....	4
1.3. Enhanced Surfaces.....	6
1.3.1. Machined Surface Enhancements.....	7
1.3.2. Porous Coated Surfaces.....	8
1.3.3. Double Enhancements.....	15
1.4. Parametric Effects.....	16
1.4.1. Pressure.....	17
1.4.2. Subcooling.....	17
1.4.3. Electric Field.....	18
<b>2.0 Experimental Facility and Technique for Surface Creation and Boiling Evaluation</b>	<b>20</b>
2.1. Electrochemical Deposition Facility.....	20
2.2. Smooth Surface Preparation.....	23
2.3. Electrochemical Deposition Technique.....	24
2.4. Pool Boiling Facility.....	26
2.4.1. Boiling Rig.....	26
2.4.2. Heat Transfer Test Section .....	28
2.5. Pool Boiling Procedure.....	33
<b>3.0 Results and Discussion of New Surfaces.....</b>	<b>36</b>
3.1. Electrochemical Deposition.....	36
3.1.1. Smooth Surface.....	36
3.1.2. Copper Deposition Surfaces.....	38
<b>4.0 Conclusions.....</b>	<b>57</b>
<b>5.0 Future Investigations.....</b>	<b>58</b>
APPENDICES.....	59
REFERENCES.....	88

## LIST OF FIGURES

"Images in this thesis/dissertation are presented in color."

<b>Figure</b>	<b>Title</b>	<b>Page</b>
<b>1.1.1.</b>	Boiling curve for a plain horizontal tube.....	3
<b>1.2.1.</b>	Magnified cross-section of a plain, smooth metallic surface.....	5
<b>1.3.1.</b>	Conceptual model of boiling in a porous matrix.....	10
<b>1.3.2.</b>	Theoretical models of (a) micro-porous; (b) porous non-conducting coated surfaces; (c) porous conducting surfaces.....	12
<b>2.1.1.</b>	Electrochemical deposition experimental set-up.....	20
<b>2.1.2.</b>	Cathode and acrylic plate stand at 30 degrees.....	22
<b>2.1.3.</b>	Electrical circuit diagram for electrochemical deposition.....	22
<b>2.2.1.</b>	Reference smooth surface.....	23
<b>2.3.1.</b>	Limiting Current Curve for Cathode at 30°.....	25
<b>2.4.1.</b>	Nucleate Pool Boiling Rig.....	28
<b>2.4.2.</b>	Partially assembled heat transfer test section.....	29
<b>2.4.3.</b>	Schematic of thermocouple positions and numbering.....	30
<b>2.4.4.</b>	Fully assembled heat transfer test section.....	32
<b>3.1.1.</b>	Reference smooth surface.....	36
<b>3.1.2.</b>	ESEM image of smooth surface at 5000x.....	37
<b>3.1.3.</b>	RMS surface roughness results for smooth surface.....	38

<b>3.1.4.</b>	<b>15° electrochemical deposition surface.....</b>	<b>42</b>
<b>3.1.5.</b>	<b>30° electrochemical deposition surface.....</b>	<b>41</b>
<b>3.1.6.</b>	<b>ESEM image of general surface structure EDS at 1000x.....</b>	<b>44</b>
<b>3.1.7.</b>	<b>ESEM image of light areas on 15° EDS at 5000x.....</b>	<b>45</b>
<b>3.1.8.</b>	<b>ESEM image of dark streak on 15° EDS at 5000x.....</b>	<b>45</b>
<b>3.1.9.</b>	<b>ESEM image of light areas of 30° EDS at 5000x.....</b>	<b>46</b>
<b>3.1.10.</b>	<b>ESEM image of dark streak on 30° EDS at 5000x.....</b>	<b>46</b>
<b>3.1.11.</b>	<b>Surface roughness data for dark streak of 15° EDS.....</b>	<b>48</b>
<b>3.1.12.</b>	<b>3-D surface roughness data for dark streak of 15° EDS.....</b>	<b>48</b>
<b>3.1.13.</b>	<b>Surface roughness data for dark streak of 30° EDS.....</b>	<b>49</b>
<b>3.1.14.</b>	<b>3-D surface roughness data for dark streak of 30° EDS.....</b>	<b>49</b>
<b>3.2.1.</b>	<b>Pool boiling curves for experimental surfaces.....</b>	<b>51</b>
<b>3.2.2.</b>	<b>Bubble formation on smooth reference surface.....</b>	<b>54</b>
<b>3.2.3.</b>	<b>Bubble formation on 30° electrochemical deposition surface.....</b>	<b>54</b>
<b>3.2.4.</b>	<b>Bubble formation on 15° electrochemical deposition surface.....</b>	<b>54</b>
<b>3.2.5.</b>	<b>Magnified schematic of possible vapor pockets on deposition surface.....</b>	<b>55</b>
<b>3.2.6.</b>	<b>Magnified schematic of possible troughs on deposition surface.....</b>	<b>58</b>

## LIST OF TABLES

<b>Table</b>	<b>Title</b>	<b>Page</b>
<b>1.3.1.</b>	Coating thickness parameters used by Chang and You.....	12
<b>3.1.1.</b>	Values of dimensionless parameters for 15° and 30° surfaces.....	40
<b>3.1.2.</b>	Values of average column-face sizes for 15° and 30° EDS.....	44
<b>3.1.3.</b>	RMS surface roughness values for 15° and 30° EDS.....	47

## LIST OF APPENDICES

<b>Appendices</b>	<b>Title</b>	<b>Page</b>
<b>A</b>	Steady-State Verification.....	60
<b>B</b>	Determination of Physical Properties.....	63
<b>C</b>	Calculation of Physical Properties.....	65
<b>D</b>	Pool Boiling Calculations.....	68
<b>E</b>	Pool Boiling Data.....	72
<b>F</b>	Uncertainty Analysis.....	86

## NOMENCLATURE

$c$	concentration of copper ions at the cathode
$C_p$	specific heat (J/kg°C)
$C_{sf}$	experimental boiling constant
$D_{Cu}$	average diffusion coefficient of the copper ions
$F$	Faraday number, 96,500 (As/g)
$g$	acceleration due to gravity ( $m/s^2$ )
$h$	heat transfer coefficient ( $W/m^2K$ )
$h_{fg}$	enthalpy of vaporization (J/kg)
$i$	current density at limiting current conditions
$k$	thermal conductivity ( $W/(mK)$ )
$k_m$	mass transfer coefficient
$L$	length (m)
$n$	valence of the copper ions
$R$	thermal resistance ( $m^2K/W$ )
$q''$	heat flux ( $W/m^2$ )
$t$	transference number
$T$	temperature (°C)
$x$	distance from the leading edge of the cathode



## **Greek Symbols**

$\alpha$	thermal diffusivity ( $\text{m}^2/\text{s}$ )
$\beta$	coefficient of thermal expansion ( $1/\text{K}$ )
$\delta$	characteristic length of heat transfer surface (m)
$\mu$	dynamic viscosity ( $\text{kg}/(\text{m}\cdot\text{s})$ )
$\rho$	density ( $\text{kg}/\text{m}^3$ )
$\sigma$	surface tension ( $\text{N}/\text{m}$ )
$\nu$	kinematic viscosity ( $\text{m}^2/\text{s}$ )

## **Subscripts**

i	surface of cathode
sub	subcooled
w	boiling surface
0	location inside OFHC copper block
1	OFHC copper
2	solder
3	surface material
$\infty$	bulk condition

# **CHAPTER 1**

## **INTRODUCTION**

Enhanced boiling surfaces are capable of producing heat transfer coefficients up to 100 times greater than that of plain, smooth surfaces. There are two ways in which a surface can enhance boiling. To be considered an enhanced boiling surface, the surface must either increase the number of boiling nucleation sites on the surface or reduce the required boiling incipient superheat. Enhanced boiling heat transfer is of great importance to the refrigeration and air conditioning industries, hydrocarbon and chemical industries, heat pipe industry, and the microelectronics industry. Advances in the microelectronics industry have produced electronic devices that require increased heat dissipation to maximize service life and reliability. Thus, interest in immersion cooling techniques for these devices, involving boiling heat transfer between the device and coolant, has grown considerably.

Enhanced surfaces are designed to initiate boiling at a lower wall superheat than that of a plain, smooth surface. The wall superheat refers to the temperature difference between the heated surface and surrounding liquid. Enhanced surfaces can be divided into two categories: machined surfaces and porous coatings. Machined enhanced surfaces contain grooves and cavities specifically designed to promote bubble formation. Porous surfaces consist of an irregular matrix of cavities produced by such methods as electrochemical deposition, sputter deposition, and sintering. This matrix provides preferred sites for bubble generation.

There are many different methods of producing porous enhanced boiling surfaces.

These different production methods result in diverse variations of the sizes, shapes, and orientation of porous coating particles. Boiling performance enhancements resulting from specific combinations of these geometric variations for a given fluid are not fully known. The objective of this work is to create and characterize a new porous surface with controlled structure variations and relate these variations to nucleate pool boiling incipience.

In this work, an electrochemical deposition experiment was designed to create porous surfaces with varying degrees of structure and particle distribution under a carefully controlled, repeatable process. This method of particle deposition produced a matrix structure of micron-sized protrusions with pores and cavities that can be preferred sites. The surfaces were examined using an environmental scanning electron microscope (ESEM) and atomic force microscope (AFM), which provided a detailed description of the character of the pores and cavities.

A pool boiling facility was designed to investigate the boiling incipience of water on the porous surfaces and on a reference smooth surface. Experimental boiling results were used to evaluate the performance of the new enhanced surfaces. Surface characterizations and boiling performance results of the porous surface are then compared to the reference smooth surface as well as other surfaces presented in literature.

## **1.1 POOL BOILING**

Pool boiling occurs on a heated surface in a large pool of quiescent liquid. Pool boiling heat transfer is typically described by plotting the surface heat flux as a function of the temperature difference between the heated surface and the surrounding bulk liquid

(wall superheat).

Figure 1.1.1 presents the classic boiling curve for boiling on the outside of a plain, smooth tube in water. The curve is divided into four distinct heat transfer regimes: single-phase natural convection, nucleate pool boiling, transition boiling, and film boiling.

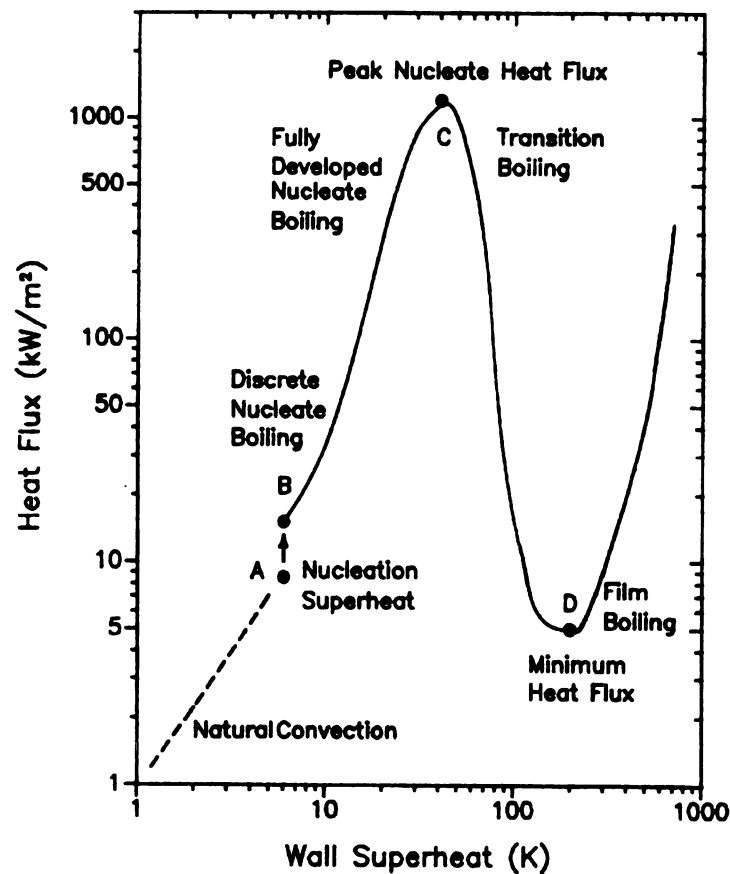


**Figure 1.1.1.** Boiling curve for a plain horizontal tube [32]

The natural convection regime exists until the point at which the first vapor bubbles form on the heated wall (boiling incipience). The temperature of the heated wall at incipience must reach a value (point A) above the saturation temperature in order for

boiling to initiate. This value is called the nucleation superheat. Once nucleation occurs, the mechanism of heat transfer changes and the heat flux passing through the heated wall increases to a higher value (point B). Nucleate pool boiling is initiated at this point. In this regime, bubbles grow and depart from the heated wall at numerous locations called nucleation sites. The new surfaces studied in this work are intended to increase the density of nucleation sites, which will in turn enhance the heat flux and reduce the wall superheat at incipience.

The wall superheat continues to rise and eventually reaches a maximum called the peak nucleate heat flux (point C). As the wall superheat is further increased, a vapor film forms over portions of the heated wall initiating transition boiling. The vapor, which greatly reduces the amount of heat being transferred from the heated wall to the fluid, continues to grow until liquid is no longer able to come in contact with the wall.

## **1.2 INCEPTION OF BOILING**

The temperature difference between a heated surface and its surrounding liquid must exceed a particular value in order for the mode of heat exchange to progress from a single-phase to a two-phase convection process. Once this certain minimum wall superheat is reached, boiling incipience occurs and is characterized by bubbles that begin to grow and depart from various sites on the heated wall. These bubbles growing and departing from the heated surface during boiling originate from preferred nucleation sites on the surface.

Numerous investigations, including [10], have demonstrated that boiling nucleation from a smooth surface occurs at microscopic imperfections in the surface.

Thome [32] states that a surface appearing to be smooth is actually covered with small cavities of various sizes, shapes, and depths (Fig. 1.2.1).

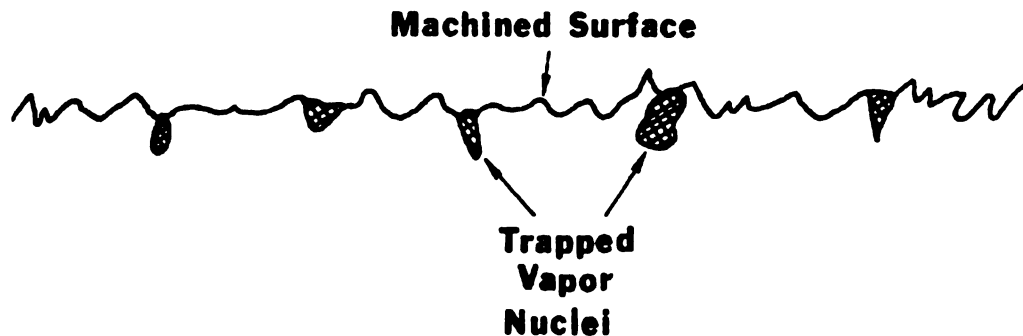


**Figure 1.2.1.** Magnified cross-section of a plain, smooth metallic surface [32]

These cavities are on the order of  $0.1\text{-}10\text{ }\mu\text{m}$  in diameter and act as nucleation sites due to their ability to trap vapor [30]. As the surface is heated the trapped vapor grows into a bubble and detaches. Once the bubble departs from the surface, a liquid film again covers the cavity where some vapor remains trapped. This remaining trapped vapor acts as an embryo for the next bubble. The criteria for vapor trapping and growth of the vapor embryo are useful in determining the wall superheat required to initiate boiling.

When boiling on a surface, the number of active nucleation sites per area is referred to as nucleation site density. Increasing the nucleation site density on a surface increases the boiling performance. Porous coated surfaces increase the nucleation site density by increasing the number of preferred bubble sites on the surface. Nucleation site density is a linear function of heat flux [15] and is also partly dependent on porous coating geometry. The simplest way to determine the number of active nucleation sites on a surface is by bubble visualization. Chein and Webb [8] determined bubble dynamics data by recording the boiling process with a high-speed photography system,

viewing more than 500 frames at 3 different surface locations, and then averaging the data.

Kim et al. [18] investigated the nucleate pool boiling heat transfer enhancement mechanism of microporous surfaces immersed in saturated FC-72. The heat transfer mechanisms associated with pool boiling were stated to be liquid convection and latent heat transfer. When comparing the plain wire to the microporous wire, it was suggested that the microporous coating appeared to augment heat transfer through increased latent heat transfer from the higher active nucleation site density. Due to its lower site density, the plain surface was said to dissipate more heat through convection heat transfer, which in turn requires a higher surface temperature to dissipate the same amount of heat as the microporous coated surface.

### **1.3 ENHANCED SURFACES**

Industrial demand for more efficient heat exchangers has spurred the development of methods to increase boiling heat transfer coefficients. A smooth plain surface can be enhanced to increase boiling heat transfer performance. Two important parameters to consider for enhancing boiling heat transfer, according to Thome [32], are boiling nucleation and nucleation site density. Boiling nucleation refers to the wall superheat required for boiling incipience and nucleation site density refers to the number of active boiling sites per area of the heated surface. In order for a boiling surface to be considered enhanced, the surface must either require a lower wall superheat for boiling nucleation or produce a higher number of active nucleation sites compared to boiling on a smooth

surface. Typically the two parameters are coupled and an enhanced surface will satisfy both conditions.

### **1.3.1 Machined Surface Structures**

Machined enhanced surfaces contain grooves and cavities designed to promote bubble formation. Examples of commercially available machined enhanced surfaces are the Turbo-BII<sup>TM</sup>-LP, GEWA-K<sup>TM</sup>, and GEWA-T<sup>TM</sup>. Bubble formation on these types of surfaces is highly dependent upon the imposed heat flux [17].

#### **Surface Characterization**

Numerous investigations focus on machined enhanced surfaces consisting of interconnected tunnels and pores. Two key geometric characteristics of the surfaces are (1) subsurface tunnels and (2) surface pores or fin gaps [6]. Chien and Webb further define these key features by the following dimensional parameters: tunnel pitch, tunnel height, tunnel width, tunnel base radius, tunnel shape, pore diameter, and pore pitch.

Chien and Webb [6], [7], and [9] identify the effects of the above geometric parameters on the boiling performance of tunneled enhanced boiling surfaces. These studies provide boiling data using R-11, R-22, R-123, and R-134a as the working fluids for an extensive variety of parameter combinations. For the fluids and geometries tested Chien and Webb found that: sharp tunnel corners provide a greater enhancement, the boiling heat transfer rate decreases as the tunnel height reduces, and the boiling coefficient is strongly influenced by pore size at a given heat flux.

In a similar study, Ramaswamy et al [27] investigated the effect of pore size, pitch, and tunnel height on the boiling performance of the highly wetting fluid FC-72. A



larger pore size and smaller pore pitch resulted in higher heat dissipation at all heat fluxes. It was noted that the effect of pore pitch on heat transfer performance was more significant than pore size.

### **1.3.2 Porous Coated Surfaces**

Porous enhanced surfaces consist of an irregular matrix of potential nucleation sites produced by such methods as welding, sintering, electrolytic deposition (method used in present investigation), flame spraying, plating, sputtering, or plasma spraying [3]. These nucleation sites promote high rates of bubble formation such that the required wall superheat for developed nucleate boiling is significantly lower compared to that required for boiling from surfaces with natural cavities [1].

A common commercially available porous enhanced surface is the High-Flux<sup>TM</sup> surface. The High Flux<sup>TM</sup> surface contains many irregular cavities similar to those of coral [17]. The thickness of the porous coating is approximately 0.645 mm and the porosity of the matrix is 45%. The particles are sintered onto the surface and form randomly shaped cavity openings that are approximately 0.04 to 0.13 mm in diameter. The High Flux<sup>TM</sup> surface provides superior boiling heat transfer performance and is often used as a benchmark for assessing boiling performance of other porous coated surfaces.

Porous coatings essentially transform heat transfer laws at bulk boiling according to the heat transfer law  $q'' \sim \theta^n$  for  $n \neq 1$  where  $\theta$  is the wall superheat [1]. Andrianov et al. [1], Kovalev [19], and Chang [4] report that boiling on porous coatings is different from boiling on plain surfaces and involves two modes. In the first mode the vapor generating zones inside the porous coating are not connected with each other. In the second mode

the vapor-filled pores are connected over the whole system. The transition from 'Bubble Mode I' to 'Bubble Mode II', terms used by Andrianov et al. [1], involves a substantial increase of the wall temperature which indicates that a continuous vapor film is formed in the vapor layer.

Bergles and Chyu [3] postulate several mechanisms of boiling from porous coatings. Consider boiling nucleation in the porous matrix shown in Figure 1.3.3. If the matrix material is poorly wetted, vapor will be retained in the interstitial space when the temperature is reduced below the saturation temperature. Alternately, with a more wetting liquid, re-entrant and double re-entrant cavities are required to permit stable dropwise formation so that the cavities are not filled with subcooled liquid. For either type of working fluid, the porous matrix increases the probability that nucleation sites are available which will remain active for repeated cycles of heating and cooling.

Bergles and Chyu postulate a vapor bubble formed in an interparticle space to be generated primarily by evaporation of the thin film segments separating the bubbles from the particles. The bubble then grows and squeezes out of a convenient pore. Fresh liquid is then supplied to vapor production centers through non-bubbling pores and interconnected channels. The total superheat is then assumed to be the sum of the conduction temperature drop across the liquid film and the traditional superheat for a curved liquid-vapor interface.

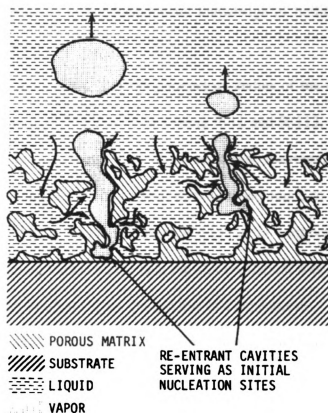


**Figure 1.3.1.** Conceptual model of boiling in a porous matrix [3].

### **Surface Characterization**

Porous layers can be characterized by the following four parameters: particle size, layer thickness, particle material, and porosity [32]. It would be desirable to determine an optimal combination of these parameters to maximize boiling performance. Within a specific set of geometries it is possible to determine an optimum layer thickness, particle diameter, or method for producing a porous layer. The optimal values found in one study only vaguely correspond to those found in other studies. Thus it is extremely difficult to identify any particular combination of porous layer parameters to obtain optimal performance [32]. Extensive research has been dedicated to investigating the boiling performance of wide varieties of porous layer geometries using different working fluids

with the intent of contributing to the fundamental knowledge of boiling within porous layers.

Nishikawa, Ito, and Tanaka [26] ran parametric studies of the effect of particle size, layer thickness, and particle material on boiling R-11 and R-113. Using spherical copper particles 0.25 mm in diameter, they observed a large maximum in heat transfer performance with layer thickness. The optimal thickness was found to be 1 mm, which corresponded to a ratio of layer thickness to particle diameter of 4 for both the copper and the bronze. At the optimum thickness, the heat transfer coefficient was a strong function of heat flux, whereas non-optimal values showed less of a dependency.

Chang and You [4] investigated particle size effects on the boiling performances of micro-porous enhanced surfaces using five different sizes of diamond particles with FC-72 as the working fluid. The thicknesses of the coatings are compared to the superheated layer thickness,  $\delta_{ss}$ , which is calculated using one-dimensional transient heat conduction. The coatings are classified into two groups: ‘micro-porous’ and ‘porous’ coatings (Fig. 1.3.4). The micro-porous coatings show different characteristics of boiling performance compared to porous coatings. Table 1.3.1 gives the values of particular coating characteristics used Chang and You’s investigation. The micro-porous surfaces correspond to the coatings with thickness  $\leq 100 \mu\text{m}$  and the porous coatings have a thickness  $> 100 \mu\text{m}$ .

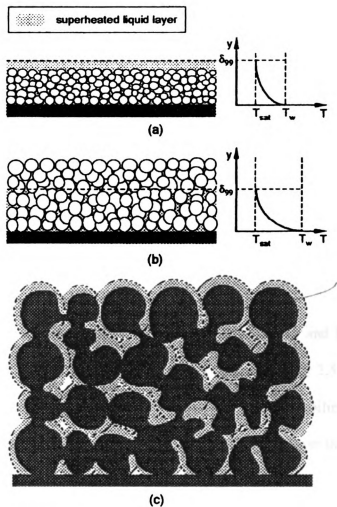


**Figure 1.3.2.** Theoretical models of (a) micro-porous; (b) porous non-conducting coated surfaces; (c) porous conducting surfaces [4].

Particle Size ( $\mu\text{m}$ )	Coating Thickness ( $\mu\text{m}$ )	Thickness/particle diameter
$2 \pm 1$	$30 \pm 10$	$\approx 15$
$10 \pm 2$	$50 \pm 20$	$\approx 5$
$20 \pm 3$	$100 \pm 30$	$\approx 5$
$45 \pm 5$	$200 \pm 50$	$\approx 4.4$
$70 \pm 10$	$250 \pm 50$	$\approx 3.6$

**Table 1.3.1.** Coating thickness parameters used by Chang and You [4].

For the micro-porous coatings, increasing the coating thickness and particle diameter resulted in an increase in active nucleation sites and a significant decrease in incipient superheat. The enhancement of heat transfer coefficient in this regime is attributed to this increase in active nucleation sites. The micro-porous coating with a thickness of 100  $\mu\text{m}$  and particle size of 20  $\mu\text{m}$  resulted in the maximum performance enhancement for the coatings tested. The thickness of this coating is close to the value of  $\delta_{99}$ . Thus an optimum coating thickness is close to the value of  $\delta_{99}$ . Note that the ratio of layer thickness to particle diameter for the optimum coating is close to the value determined by Nishikawa et. al [26].

For the porous coated surfaces, increased particle diameter and layer thickness resulted in higher heat transfer coefficients at lower heat fluxes ( $\leq 2.5 \text{ W/cm}^2$ ). For higher heat fluxes the trend was reversed. This trend in nucleate boiling performance was attributed to increased thermal resistance due to an increase in layer thickness as well increased hydraulic resistance over liquid-vapor exchange channels.

Chang and You [5] also investigated the effect of coating composition (particle material) on the boiling performance of optimized micro-porous coatings again using FC-72 as the working fluid. Four different micro-porous coatings were created using the following particles: aluminum, copper, diamond, and silver. The coatings had a layer thickness to particle size ratio of between 4 and 5. The experimental boiling data for the four coatings practically collapsed onto one curve. Thus the boiling performance of the coatings is independent of particle composition.

The boiling performance of these coatings was compared to a plain uncoated reference surface. The micro-porous coatings resulted in 80-90% reductions in incipient

superheats and a 30% increase in heat transfer coefficient. Again the performance enhancement of the micro-porous coatings was attributed to increased nucleation site density. These coatings were also compared to High Flux commercial porous coating. The performance of the micro-porous coatings was not as good as the High Flux coating.

Hsieh and Ke [15] investigated boiling on porous Copper and Molybdenum plasma coated tubes. They introduced a geometric scale factor  $\lambda = \eta/\delta$  where  $\eta$  is the average pore diameter (related to porosity) and  $\delta$  is the coating thickness. These two parameters were deemed to have the most influence on heat transfer performance, in a similar investigation by Hsieh and Yang [14], and determine the probability of flooding of re-entrant cavities and the degree of superheat required for bubble growth. The values of  $\lambda$  for the Copper and Molybdenum tubes were 0.01 and 0.04 respectively. The Copper sample resulted in a larger nucleation site density for the fluids tested. Also, for the three surfaces tested, the nucleation site density was greater for R-134a than for R-600. The two fluids have similar surface tension values, but significantly different values of enthalpy of vaporization and density. The enthalpy of vaporization of R-134a is nearly half that of R-600. The density of R-134a is double that of R-600.

Mertz et al. [24] investigated the effect of thickness and porosity on the boiling of propane on stainless steel tubes with flame-sprayed porous coatings. The thickness of the porous layers range from 100 to 300  $\mu\text{m}$  and the porosities range from 4% to 17%. It was noted that there is a distinct influence of porous coating thickness and porosity on the heat transfer coefficient. For thicknesses equal to 100, 150, 200 and 300  $\mu\text{m}$  with the same porosity (12.7%), the coating with a thickness of 200  $\mu\text{m}$  resulted in the highest heat transfer coefficient. Lower porosities resulted in lower heat transfer coefficients for

the surfaces tested.

Webb [33] explains the differences in performance of porous layers of varying porosities on the basis that different types of pores produced:

1. Active pores with stable nucleation sites
2. Intermittent pores, which can be filled with either liquid or a vapor meniscus depending on the type of flow present in the porous matrix.
3. Liquid-filled pores that act to supply superheated liquid to the active and intermittent pores.
4. Nonfunctional pores, that are closed voids containing neither boiling liquid nor vapor.

Andrianov et. al. [1] defines the radius of steam evacuation ( $R_1$ ) as a porous coating characteristic and an integral feature of nucleation site operation. In bubble mode I, where the greatest increase of heat transfer is achieved compared to a smooth surface, steam evacuation sites work independently where  $R_1$  is constant and approximately equal to the thickness of the coating. With an increase in heat load up to the transition from bubble mode I to II,  $R_1$  rapidly increases, then decreases with further increases in heat load. This decrease of  $R_1$  is compensated by the growth of the number of working steam exit sites.

### **1.3.3 Double Enhanced Surfaces**

Recently, Rainey and You [28] investigated the effects of surface ‘double enhancements’ on nucleate pool boiling performance. Rainey and You combined a surface enhancement (microporous coating) and an area enhancement (square pin-fins)



on 1 cm<sup>2</sup> flush mounted copper surfaces. Porous coated pin-fins with lengths of 1, 2, 4, and 8 mm were tested and compared to surfaces with plain fins of the same lengths and a flat microporous surface. All tests were performed in saturated FC-72 at atmospheric pressure under increasing heat flux conditions. The microporous coated finned surfaces provided significantly higher heat transfer coefficients over the plain finned surfaces and resulted in slightly lower incipient superheats. Interestingly, the nucleate boiling data for the coated finned surfaces collapse to one curve when plotted relative to the flat microporous surface regardless of fin length (up to 8 mm). This shows that the nucleate boiling heat transfer coefficient (based upon a given base area) can be increased with the application of a micro-porous coating, however, no further improvement is gained by increasing the fin length. It is also interesting to note that for the tests with the plain finned surfaces, increasing the fin length significantly changes the results in the natural convection regime.

Honda et al. [11] compared the boiling performance of FC-72 on a square silicon chip with micro-pin-fins and a chip of the same base size with submicron scale roughness. The flat chip with the submicron-scale roughness showed a higher heat transfer performance than the micro-pin-finned chip in the low-heat-flux region. This trend was reversed in the high-heat-flux region.

#### **1.4 PARAMETRIC EFFECTS**

For pool boiling heat transfer investigations, the experimental setup and methodology directly influence heat transfer measurements. Particular attention must be given to parametric effects for accurate boiling measurements and comparisons.

### **1.4.1 Pressure**

Boiling curves for plain surfaces move to the left with increasing pressure [32]. Thus conventional boiling performance increases with rising pressure. Rainey et al. [29] report that the incipient superheat increases with decreasing pressure. They also found that the difference in the nucleate boiling performance between the plain and microporous surfaces appears to decrease with increased pressure.

### **1.4.2 Subcooling**

When boiling occurs on a heated surface and the bulk liquid is at a temperature lower than its saturation temperature, subcooled boiling occurs. Generally, the boiling curve moves to the right as subcooling increases [32]. For boiling on plain surfaces, the boiling heat transfer coefficient drops off rapidly with increased subcooling [32]. Bajorek [2] investigated the effect of subcooling on boiling on a low-finned copper tube. He obtained data for water, ethanol, and several mixtures at atmospheric pressure for subcooling ranging from 0 – 40 K. He found that the largest drop in the heat transfer coefficient occurred in the first 10 K of subcooling. In this range, boiling performance was reduced by 40% to 50%.

Rainey et al. [29] investigated the effect of subcooling on boiling on plain and microporous flat copper blocks immersed in FC-72. They felt the most prominent effect of subcooling on boiling was that the fully developed nucleate boiling curves collapsed onto a single line regardless of the degree of subcooling. The insensitivity of the nucleate pool curve to increased subcooling is attributed to the combined effects of (1) reduced bubble departure diameters and frequencies leading to reduced amounts of heat

transferred through latent heat and microconvection and (2) decreased superheated liquid layer thickness leading to increased natural and Marangoni convection heat transfers.

### **1.4.3 Electric Field**

Leontiev et. al. [20] investigated the effect of an electric field on the boiling of liquid nitrogen. An electrode with a 30 kV potential was placed 3 mm above the test surface. Both uniform and non-uniform electric fields were tested on horizontal smooth and corrugated surfaces. The uniform electric field, with an intensity of up to  $10^7$  V/m, had little or no effect on the initial part of the boiling curve of the smooth surface. The non-uniform electric field was created by welding a metallic pin near the test surface. With the presence of the non-uniform electric field, both the smooth and corrugated surfaces showed a reduction on incipience superheat as compared to the results with the uniform electric field.

Snyder et al. [31] performed an experiment to produce a dielectrophoretic (DEP) force (up to 23 kV) over the length of a horizontal platinum wire heater (1.91 cm by 0.025 cm diameter). It was concluded that the overall boiling heat transfer coefficient in the presence of an electric field can be modeled as the summation of a heat transfer coefficient due to bubble dynamics and a heat transfer coefficient due to electroconvection. The heat transfer in the presence of an electric field will be enhanced if the effective gravity acts to hold the vapor bubbles near the heated surface, while at the same time permitting access of the liquid to the surface in order to prevent dryout. The work done by Leontiev et. al. [20], as discussed above, reported that a non-uniform electric produced areas, called “field traps”, where the dielectrophoretic forces trap

growing bubbles on the heated surface. Maximum local heat transfer coefficients were observed for the areas with the presence of field traps.

## CHAPTER 2

### EXPERIMENTAL FACILITY AND TECHNIQUE FOR SURFACE CREATION AND BOILING EVALUATION

#### 2.1 ELECTROCHEMICAL DEPOSITION FACILITY

The test environment for the electrochemical deposition consisted of an electrolyte solution in a 204 liter polyethylene tank as shown in Figure 2.1.1. The anode, cathode, and reference electrode were immersed in the electrolyte solution and connected to a series of potentiometers, digital multimeters (DMM) and a DC power supply. The cathode was the test surface for deposition.

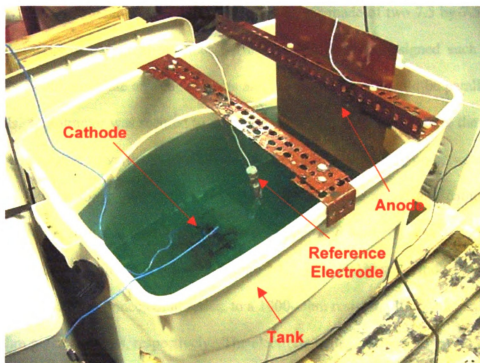


**Figure 2.1.1.** Electrochemical deposition experimental set-up.

The tank was a 81 by 50 by 50 cm Rubbermaid container. The bottom of the tank was made horizontal as measured with a precision level. The tank was filled with an electrolyte solution consisting of aqueous solutions of 1.5 molar reagent grade sulfuric

acid ( $\text{H}_2\text{SO}_4$ ) and 0.05 molar copper II sulfate ( $\text{CuSO}_4$ ). The copper ions of the  $\text{CuSO}_4$  served as the transferred species of ions and the  $\text{H}_2\text{SO}_4$  was the supporting electrolyte.

The anode and cathode were constructed from 0.32 cm thick copper sheets with dimensions 54.3 by 30.5 cm and 6.0 by 7.5 cm respectively. The anode surface area was 34 times larger than the surface area of the cathode to insure that the electrode reaction would be controlled by the cathode. The reference electrode was made by inserting 14 gauge copper wire into a polyethylene test tube with a capillary hole drilled in the bottom.

The cathode was held approximately 1.3 cm off the bottom of the tank, facing the anode by an acrylic stand. The stand, Figure 3.1.2, was made of two 7.5 by 7.5 by 0.64 cm thick pieces of acrylic sheet stock. The plate holder was designed such that the sidewalls would eliminate any edge effects and the flow of ions would be parallel to the sidewalls. A protractor was secured to one side of the plate stand to measure the angle of the cathode relative to vertical. The cathode was held in place facing up between acrylic plates by 8.9 cm long, 0.64 cm diameter brass bolts. The anode and cathode were connected to the electrical circuit with 14 gauge copper lead wire.

The electrical circuit is shown in Figure 2.1.3. The DC power supply was a deep cycle 12 Volt battery connected, in series, to a 1000-Ohm resistor, plus 0-200, and 0-1000 Ohm potentiometers, respectively. The electrode voltage and current were monitored and recorded with the DMMs.

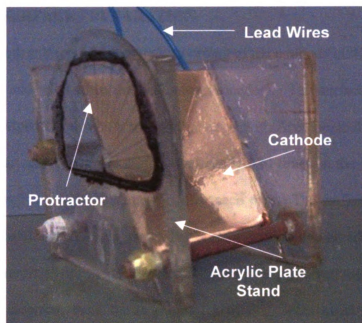


**Figure 2.1.2.** Cathode and acrylic plate stand at 30 degrees.

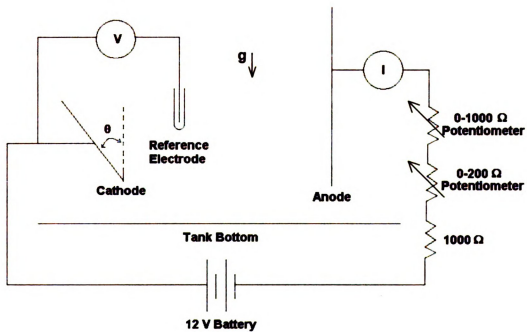


**Figure 2.1.3.** Electrical circuit diagram for electrochemical deposition.

## 2.2 SMOOTH SURFACE PREPARATION

The smooth surface was prepared according to the methods outlined by Hong [12] and Shakir [30] and adhered to the following procedure. The surface was rinsed with distilled water, wiped clean with a soft cloth, rinsed with Acetone, and wiped dry again. Using the 600-grit sandpaper, the surface was sanded 20 times in the vertical direction, bottom to top, pressing with the same force for each pass. The surface was then wiped with a soft cloth and turned 90 degrees. The surface was sanded an additional 20 times, bottom to top, pressing with the same force for each pass. The surface was wiped again and turned 270 degrees, back to its original position. This sanding technique was repeated 4 times for the 600-grit paper. The surface was then rinsed with distilled water, wiped clean, rinsed with acetone, and wiped dry again. Then 1000 grit and then 1500 grit sandpapers were used, respectively, repeating the technique above, thus producing a smooth, mirror finish as shown in Figure 2.1.4.

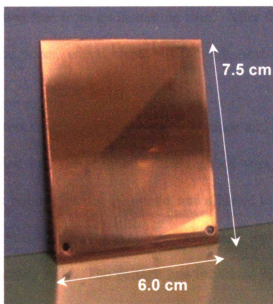


**Figure 2.2.1.** Reference smooth surface.



## **2.3 ELECTROCHEMICAL TECHNIQUE**

The electrochemical deposition procedure is consistent with that of Lloyd [20]. To eliminate concentration gradients, the electrolyte solution was stirred for approximately 30 minutes prior to placing the test surface in the tank. A Type-T thermocouple was used to measure and verify the uniformity of the solution temperature. The temperature was measured along the bottom of the tank, two-thirds from the top, one-third from the top, and near the surface totaling 20 different locations throughout the solution. The solution temperature was considered uniform if the measurements did not vary by more than 0.5 degrees Celsius as stated by Moran [25].

Before each run, a cathode surface was prepared for deposition by completing the sanding regiment presented in Section 3.2 to produce a smooth surface. Once a smooth, mirror surface was obtained, the back of the cathode was insulated with duct tape. The cathode was then secured to the acrylic plate stand and the lead wires were attached.

The anode was sanded with coarse sandpaper on the front and back surfaces to insure that the surface was free from an insulating film. After the surface was sanded it was rinsed with distilled water, wiped clean, rinsed with Acetone, and then wiped dry again.

The potentiometers were set at maximum resistance and the anode and reference electrode were suspended into the solution. The cathode was carefully placed on the level portion of the tank bottom, facing the anode, and allowed to set for 20 minutes. The lead wires were connected, completing the electrical circuit, and the voltage and current were allowed to reach steady state. The voltage was increased by incrementally reducing the 0-1000 Ohm potentiometer resistance. Once the resistance was reduced, the solution

was allowed to reach steady state and the voltage and current readings were recorded. The voltage was increased until the characteristic limiting current curve was achieved (Fig. 2.3.1).

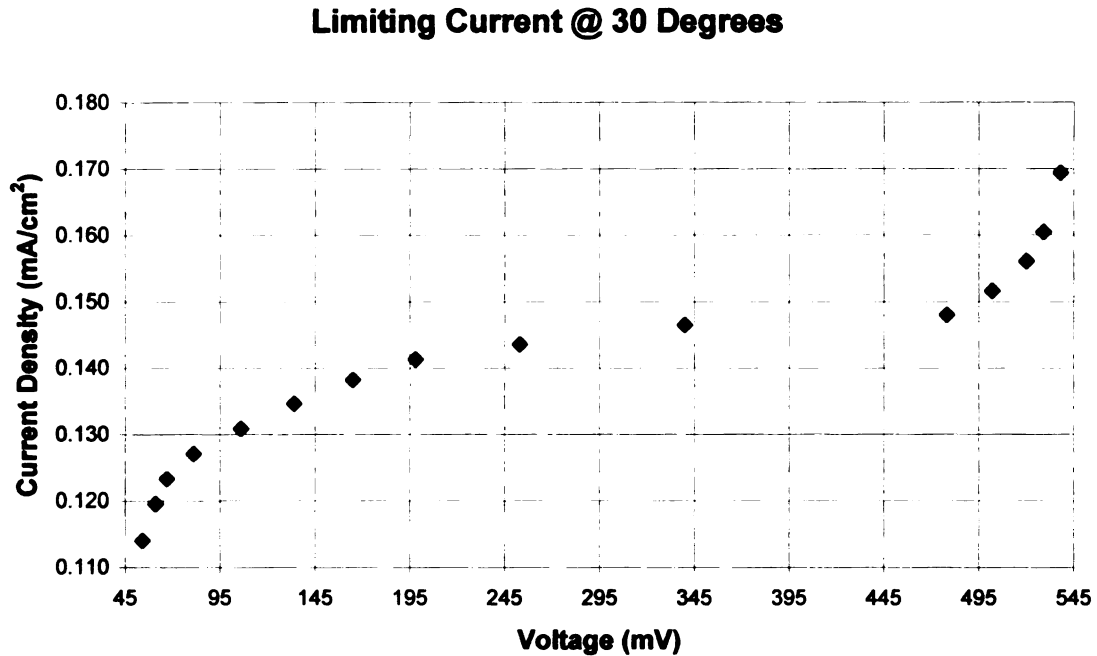


**Figure 2.3.1.** Limiting Current Curve for Cathode at 30°.

The plateau region of the limiting current curve is the condition where diffusion of the copper ions controlled the mass transfer of the copper deposition process. Once the nominal current value of the plateau of the limiting current curve was determined, the electrode voltage was set to produce this current. The cathode was then allowed to set at this current for 2 hours to be consistent with the procedure used by Moran [25].

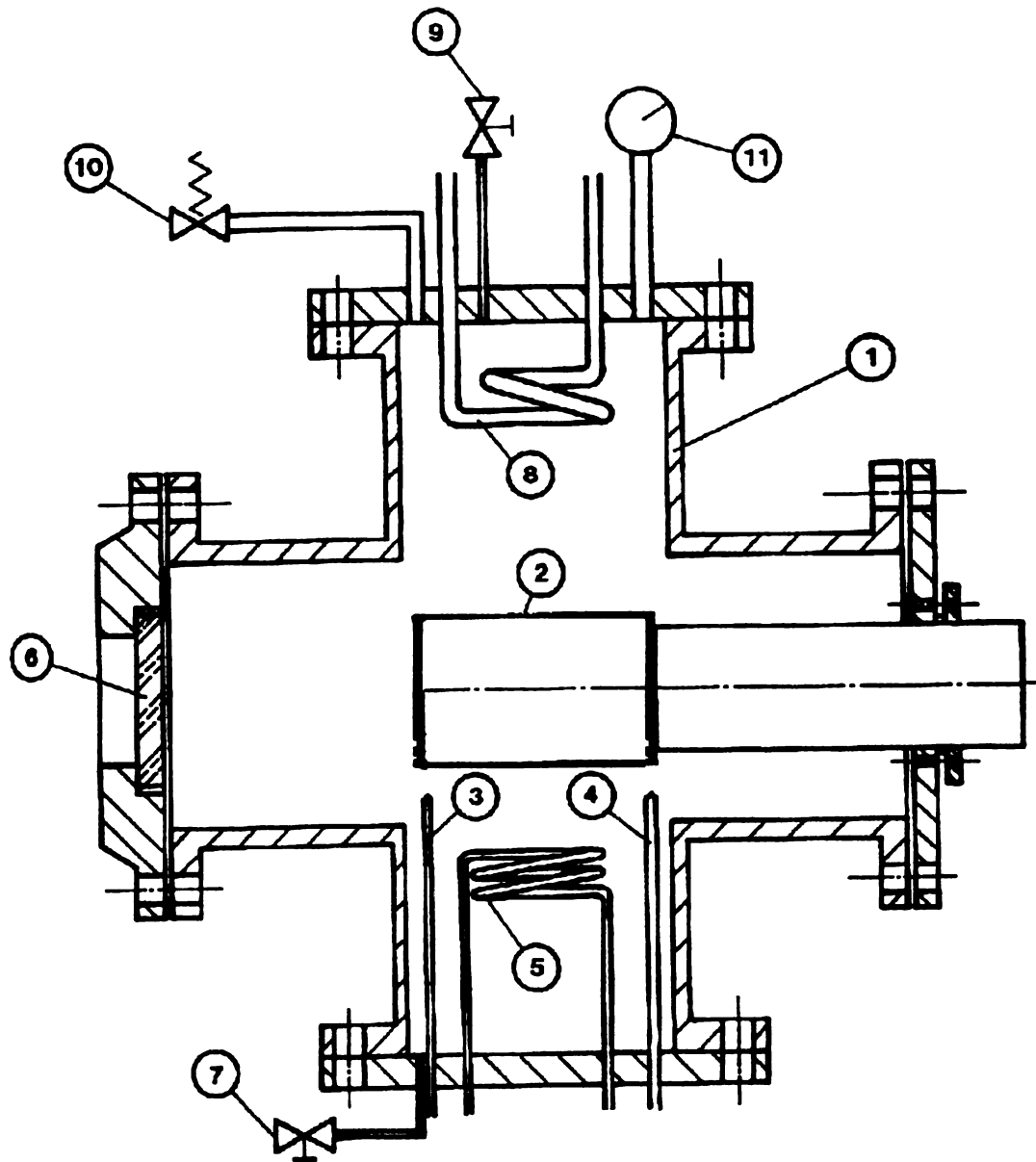
## **2.4 POOL BOILING EXPERIMENTAL FACILITY**

### **2.4.1 Boiling Rig**

A steel pressure vessel, built and developed at Michigan State, was used for the experimental studies of nucleate pool boiling. This apparatus, shown in Figure 2.4.1, was used to obtain boiling incipience superheats and heat transfer coefficients.

The pressure vessel, shown schematically in Figure 2.4.2, is a 2.54 cm thick stainless steel chamber with flanged ends. The diameter of each of the flanged ends is 10.16 cm. The volumetric capacity of the vessel is 4 Liters. The top and bottom openings were bolted with 2.54 cm thick stainless steel cover plates. Each of these cover plates had a series of openings to install the necessary attachments. A third opening was a side-flange used for mounting the test section. The fourth opening was a side-flange equipped with a viewing port made of high-quality glass (Fig. 2.4.1(6)). The vessel assembly was mounted on a rugged tripod assembly capable of rotating and tilting the rig to any desired position. To minimize heat loss through the chamber walls, the vessel was covered with 0.635 cm thick polyethylene foam insulation.

A 1350-watt immersion heater (Fig. 2.4.1 (5)), mounted at the bottom of the chamber was used to heat the liquid pool to saturation conditions. The heater was coiled from a 0.635 cm O.D. straight length of a Chromalox incoloy sheath heater and powered by a Variac variable AC power supply. Two 30-gage Type-T stainless steel sheathed thermocouples (Fig. 2.4.1 (3,4)) were mounted through the bottom cover plate of the chamber to measure the temperature of the bulk liquid. An Omega HHP-102F pressure transducer read the chamber pressure via the pressure tap mounted on the top cover plate of the chamber (Fig. 2.4.1 (11)).



- |                             |                         |
|-----------------------------|-------------------------|
| 1. Boiling Vessel           | 7. Liquid Feed Line     |
| 2. Boiling Test Surface     | 8. Condenser            |
| 3. Bulk Liquid Thermocouple | 9. Degassing Line       |
| 4. Bulk Liquid Thermocouple | 10. Safety Relief Valve |
| 5. Immersion Heater         | 11. Pressure Tap        |
| 6. Site Glass Window        |                         |

**Figure 2.4.1. Nucleate Pool Boiling Rig.**

A submersible pump was used to pump liquid through the liquid feed line and into the chamber (Fig. 2.4.1 (7)). A valve, located along the liquid feed line, was closed once the liquid had reached the desired level in the vessel. The condenser (Fig. 2.4.1 (8)) was mounted to the top cover plate of the chamber and consisted of 0.635 cm O.D. stainless steel tubing. Cold tap water was run through the coiled condenser tube during boiling. A pressure safety valve (Fig. 2.4.1 (10)) was mounted to the top of the chamber to relieve any accidental overshoot of pressure inside the vessel. A second valve (Fig. 2.4.1 (9)) was mounted to the top of the chamber for degassing purposes.

#### **2.4.2 Heat Transfer Test Section**

Kedzierski and Worthington [16] presented a technique specifically designed for building an accurate, uniform temperature boiling heat transfer apparatus. A flat plate was used as the heat transfer specimen as opposed to round tubes, as was done by Bajorek [2] because more thermocouples could be spaced parallel to the heat flow in a thick plate than in a thin-walled tube. This arrangement of thermocouples allows for simultaneous measurement of wall superheat and surface heat flux values. Copper was the suggested heat transfer material since it has a very high thermal conductivity, and the temperature profile within the block could be assumed to be linear for the calculations of both the heat flux and surface temperature. The use of 0.053 cm diameter thermocouple holes was recommended to minimize hole position uncertainty. The heat transfer test section used in this work was designed based on the Kedzierski and Worthington [16] and Kedzierski [17] studies.

The heat transfer test section used in this work consisted of the boiling test surface, a thick copper block with a series of fourteen embedded thermocouples, and another thick copper block containing three cartridge heaters. The test surface was soldered on top of the copper block housing the thermocouples, which was soldered to the top of the copper block with the heater cartridges. The heater cartridges were used to heat the test surface while the thermocouples were used to simultaneously measure the surface temperature of the boiling surface as well as the heat flux. The sides and bottom soldered copper blocks and test block were insulated with a Teflon sleeve. Figure 2.4.2 shows the stacked copper blocks (without the test surface) and Teflon sleeve with the front cover removed.

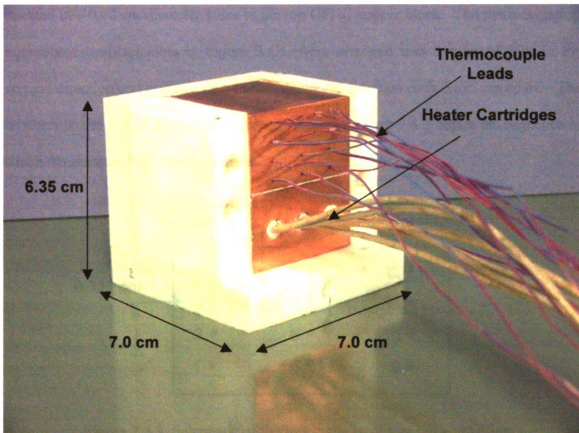


**Figure 2.4.2.** Partially assembled heat transfer test section.

Two 4.45 x 4.45 x 2.54 cm thick oxygen free high conductivity (OFHC) copper blocks, stacked and soldered one on top of the other with 60/40 tin/lead solder, were used to transfer heat from the heat source to the test surface. The bottom OFHC copper block housed three 0.635 cm diameter by 3.81 cm long 125-Watt Chromalox model CIR-1015 heater cartridges. The heaters, used to heat the test section, were first coated with Chromalox Boron Nitride Lubriccoat and then inserted into pre-drilled tight-fitting holes in the OFHC copper. The holes were drilled 0.635 cm from the edge of the copper and 0.635 cm apart centering the heaters with respect to the test section. Fourteen 30-gage 0.075 cm diameter Type-T thermocouples were used to measure the surface temperature of the test section and heat flux. The temperature sensing ends of thermocouples were inserted into 0.08 cm diameter holes in the top OFHC copper block. The thermocouples, represented by black dots in Figure 2.4.3, were arranged into 3 rows of four in the vertical direction and one row of 5 in the horizontal direction each 0.635 cm apart. The numbers to the left of the thermocouple positions in Figure 2.4.3 depict the sequence in which temperature readings were taken.

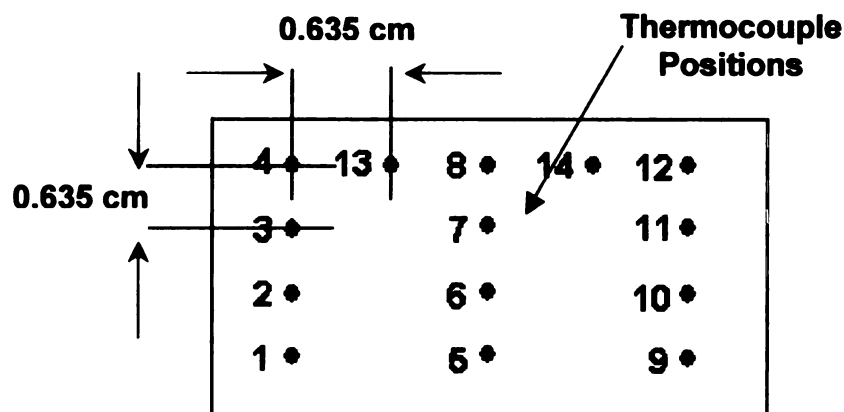


**Figure 2.4.3.** Schematic of thermocouple positions and numbering.

Once the thermocouples and heater cartridges were in place, the copper blocks were inserted into a partially assembled Teflon sleeve (as shown in Fig. 2.4.2). The fully assembled Teflon sleeve consisted of 6 cut and milled pieces of 1.27 cm thick Teflon bolted together to fit tightly around the copper blocks. Two front cover pieces were drilled and tapped to be able to connect to a threaded brass male-female adaptor. The brass adaptor connected to a 2.7 cm O.D. by 20 cm long threaded stainless steel tube. The two front cover pieces were bolted to the assembled side pieces of the sleeve. The thermocouple and heater cartridge lead wires exiting the sleeve through the tapped hole. The lead wires were held in place and insulated with General Electric RTV 106 high temperature silicone rubber adhesive sealant. Sealant was applied to the area on copper block directly surrounding the wires and was approximately 2 cm thick. The unsealed length of the lead wires was strung through the brass adaptor and stainless steel tube. The brass adaptor was then screwed into the tapped hole of the insulating sleeve as shown in Figure 2.4.4. Special care was taken not to twist the lead wires while attaching the brass adaptor to the insulating sleeve.

The stainless steel tube was used to support the heat transfer test section in the boiling rig and allowed the lead wires from the thermocouples and heater cartridges to exit the rig without coming into contact with the water. The diameter of the end of the stainless steel tube (not attached to the test section) was reduced using a lathe to be able to fit through the existing 2.5 cm hole in the side cover plate of the boiling rig.



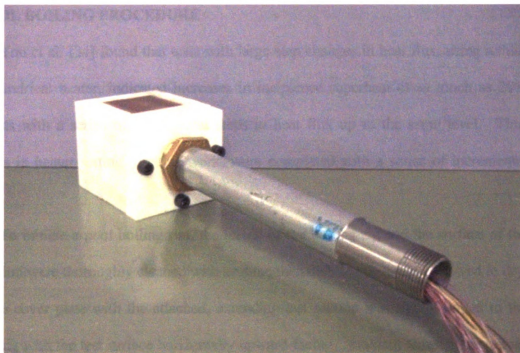


**Figure 2.4.4.** Fully assembled heat transfer test section.

Once the test section was assembled as shown in Figure 2.4.4, the test surface, cut to 4.45 cm x 4.45 cm, was soldered to the exposed copper. When the solder had cooled sufficiently, the entire assembly was then sealed with Perfecto 100% clear silicone rubber aquarium sealant. The lathed end of the stainless steel tube extending from the heat transfer test section was placed through the hole in the boiling rig side cover and sealed with the aquarium sealant. The steel tube fit very tightly through the hole in the cover plate providing ample support to the test section. More aquarium sealant was used to seal the steel tube to the cover plate.

## **2.5 POOL BOILING PROCEDURE**

You et al. [34] found that tests with large step changes in heat flux, using a thin-film cylindrical heater, indicated increases in incipience superheat of as much as 20% over tests with a series of incremental steps in heat flux up to the same level. Thus increases in heater setting, for this work, were completed with a series of incremental steps.

To initiate a pool boiling run, the inside of the boiling rig and the surface of the test section were thoroughly cleaned with acetone then distilled water and allowed to dry. The side cover plate with the attached, extending test section was tightly bolted to the boiling rig with the test surface horizontally upward-facing. Ambient temperature values of the 16 thermocouples (14 embedded in the OFHC copper block and 2 secured to the chamber) were then recorded. All of the thermocouples displayed the same temperature and ensured the accuracy of the temperature readings. Distilled water was then pumped into the rig via the liquid feed line with only the degassing valve open. Once the water was sufficiently above the condenser, the valve to the liquid feed line closed and the pump was turned off.

The immersion heater was turned on and the liquid was heated to 100 °C. The cartridge heaters were then turned on to a moderate setting of 40, corresponding to a heat flux of approximately  $15000 \text{ W/m}^2$ , and the surface was allowed to boil for approximately 30 minutes. The degassing valve was then closed and the immersion heater was turned off. The foam insulation was removed from the outside of the chamber and the condenser was turned on. The liquid was allowed to cool to 45 °C as recommended by Bergles [3]. Extra care was taken during cool-down to maintain the

pressure at its saturation value of 1.01 bar by controlling the flow through the condenser. Once the liquid had cooled, the foam insulation was returned to the boiling chamber. The immersion heater was turned back on and again the pressure maintained at 1.01 bar by controlling the water flow through the condenser. The water flowing through the condenser was chilled with an ice bath. Once the liquid was heated to 90 °C (10 degree subcooling), the heater cartridges were turned on to a low setting. A subcooling of 10° was determined as the boiling condition due to immersion heater difficulties. The system was then allowed to reach steady-state.

The temperatures from the embedded thermocouples were then recorded by dialing through the values displayed on the Omega Trendicator to the tenth of a degree. If the temperature displayed bounced back and forth between tenths of degrees, the recorded temperature was the average of the varying values. If there was no temperature variation, the displayed temperature was recorded. Power to the heater cartridges was then increased in increments of 5 on the Variac and the process was repeated until nucleate boiling was achieved. The time delay between temperature readings was 15 minutes. This amount of time was determined sufficient for steady-state conditions by experimental verification (see Appendix A).

Bubble growth was recorded during the pool boiling experiments by positioning a JVC digital video camera on a tripod in front of the glass-viewing window of the chamber. A 500-Watt lamp was positioned on a tripod next to the digital video camera to illuminate the test surface. Once the test section was secured to the chamber and a run was initialized, the lamp and video camera were positioned to provide the best image possible. Once very small bubbles began to form on the surface the lamp and video

camera were turned on and bubble growth was recorded. The lamp and camera were periodically turned off to avoid any heating of the liquid by the heat of the lamp. Thus bubble growth was watched diligently. Special care was taken to record initial bubble growth and departure.

## CHAPTER 3

### RESULTS AND DISCUSSION

#### 3.1 ELECTROCHEMICAL DEPOSITION

##### 3.1.1. Smooth Surface

The smooth surface, as prepared according to Section 2.2 has a shiny, mirror-like finish (Fig. 3.1.1.).

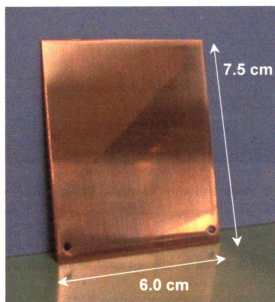


**Figure 3.1.1.** Reference smooth surface.

The smooth surface was examined with an ElectroScan Environmental Scanning Electron Microscope (ESEM) model 2020. Figure 3.1.2 shows the surface magnified at 5000x. Very fine scratches are present on the surface as a result of the surface preparation. The spans of the fine scratches were measured using the length scale provided on the ESEM image and vary from 0.85 to 2.55  $\mu\text{m}$ .

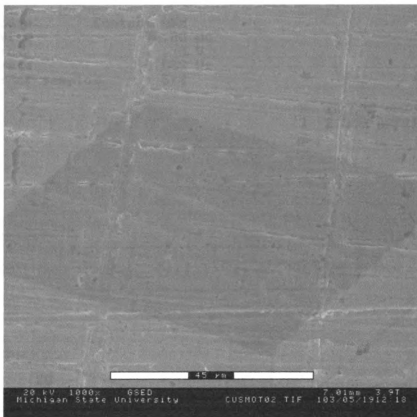


**Figure 3.1.2.** ESEM image of smooth surface at 5000x.

The RMS surface roughness was measured using a Digital Instruments Atomic Force Microscope (AFM). The RMS surface roughness is the standard deviation of the Z values, Z referring to the vertical direction, within a given area. The RMS surface roughness values were measured at three different locations using a scan size of 70  $\mu\text{m}$ . The averaged RMS surface roughness of the smooth surface was 76 nm. Figure 3.1.3 displays the 3 dimensional results from the AFM.

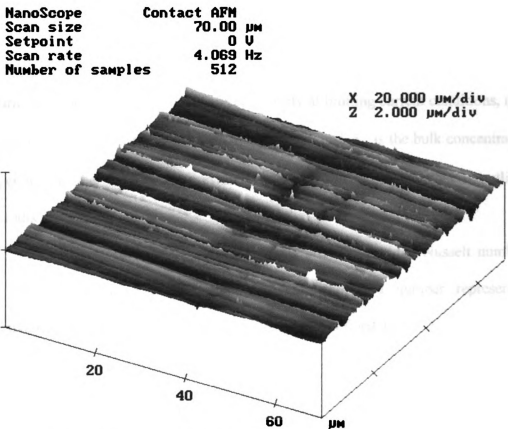


**Figure 3.1.3.** RMS surface roughness results for smooth surface.

### 3.1.2 Copper Deposition Surfaces

The principle mechanisms for the transfer of copper ions to the cathode surface are migration, diffusion and convection. Using the known values of temperature of the solution, copper ion concentration, sulfuric acid concentration, limiting current, and characteristic length of the test surface, dimensionless numbers to describe the flow over the plate during deposition can be determined. The following discussion of dimensionless parameters is consistent with that used by Lloyd [20].

Under limiting current conditions, the concentration of copper ions at the surface is negligible. Thus, the expression for the mass transfer coefficient is

$$k_m = \frac{(1-t) \cdot i}{n \cdot F \cdot c_\infty} \quad (3.1.1)$$

where  $t$  is the transference number for the copper ions at the average copper sulfate and sulfuric acid concentrations,  $i$  is the current density at limiting current conditions,  $n$  is the valence of the copper ions,  $F$  is the Faraday number, and  $c_\infty$  is the bulk concentration of copper ions at the cathode. The evaluation of the transference number is outlined in Appendix B.

The dimensionless mass transfer module, analogous to the Nusselt number for heat transfer, is the Sherwood number. The Sherwood number represents the effectiveness of mass convection at the surfaces and is defined as

$$Sh_x = \frac{k_m x}{D_{Cu}} \quad (3.1.2)$$

where  $x$  is the distance from the leading edge of the cathode to the point of interest and  $D_{Cu}$  is the average diffusion coefficient of the copper ions in the sulfuric acid. The diffusion coefficient is evaluated at the specific deposition temperatures (Appendix B).

The Rayleigh number is the product of the Grashof and Schmidt numbers as shown in Equation 2.4.3.

$$Ra_{x,\theta} = Gr_{x,\theta} \cdot Sc \quad (3.1.3)$$

The Grashof number is defined as

$$Gr_{x,\theta} = \frac{g \cdot \cos \theta \cdot (\rho_\infty - \rho_i) \cdot \rho \cdot x^3}{\mu^2} \quad (3.1.4)$$

where  $g$  is the acceleration due to gravity,  $\cos \theta$  is the cosine of the angle of the cathode measured from vertical, and  $\mu$  is the average dynamic viscosity of the electrolyte solution.



The values of  $\rho_{\infty}$ ,  $\rho_i$  and  $\rho$  are the densities of the solution in the bulk, at the surface, and at average conditions respectively.

The Schmidt number, analogous to the Prandtl number, is defined as

$$Sc = \frac{\mu}{\rho \cdot D_{CU}} \quad (3.1.5)$$

and represents the relative magnitudes of molecular momentum and mass diffusion in the velocity and concentration boundary layers respectively. Again, property evaluations are outlined in Appendix B.

According to Lloyd et. al. [22], for  $Sc \approx 2000$ , the Sherwood number can be calculated based on the Rayleigh number as a function of inclination angle as follows

$$Sh_{x,\theta} = 0.499 Ra_{x,\theta}^{1/4} \quad (3.1.6)$$

This equation is for laminar flow over the plate. The transition from laminar to turbulent flow is based on the Rayleigh number. Laminar flow exists for  $Ra < 10^{11}$  where turbulent flow exists for greater values of  $Ra$ . The flow in this work was considered laminar.

Calculated values of the dimensionless parameters for the electrochemical deposition surfaces can be found in Table 3.1.1. The Schmidt numbers correlate well to the work done by Lloyd et. al. [22] and Moran [25] and are approximately 2000. The Rayleigh number is on the order of  $10^6$  thus the flow can be considered laminar. The Sherwood numbers based on the transference of copper ions and the Rayleigh number, calculated using Equations 3.1.5 and 3.1.6 respectively, agreed within 1% for both deposition surfaces. This validates the experimental set-up and procedure discussed in Sections 2.1 and 2.3. Detailed information regarding values used to calculate these parameters can be found in Appendix C.

<i>Dimensionless Parameter</i>	<i>15°</i>	<i>30°</i>
Sc	1894	1773
$Gr_{x,\theta}$	$1.09 \times 10^7$	$1.02 \times 10^7$
$Ra_{x,\theta}$	$2.07 \times 10^{10}$	$1.86 \times 10^{10}$
Sh	224	217
$Sh_{x,\theta} (Ra_{x,\theta})$	189	184

**Table 3.1.1.** Values of dimensionless parameters for 15° and 30° surfaces.

The appearance of the electrochemically deposited surfaces (EDS) is very different from that of the smooth surface shown in Figure 2.4.1. The deposited surfaces, shown in Figures 3.1.4 and 3.1.5, appear matte-like as opposed to shiny and are accompanied by the presence of dark colored streaks near the top. These streaks are approximately 1 mm wide and 1 mm apart, corresponding to the spanwise dimensions determined by Lloyd [23], and result from longitudinal vortices that develop along the surface during deposition. These vortices are characteristic of natural convection on upward facing surfaces at angles of 14 - 45° [21]. At inclination angles less than 14° from vertical, wave instabilities dominate flow along the plate. As the inclination angle increases from 14°, the outward normal force on the plate increases and longitudinal vortices begin to dominate the flow. At 15°, the flow is governed by both wave instabilities and longitudinal vortices. As the plate angle is increased from 15 to 30°, the longitudinal vortices dominate the flow. Hence the streaks are more pronounced on the 30° plate than the 15° plate. The streaks present on the electrochemical deposition surfaces result in spanwise mass transfer variations.

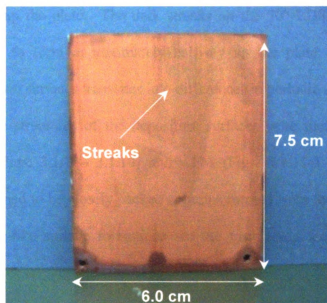


**Figure 3.1.4.** 15° electrochemical deposition surface.

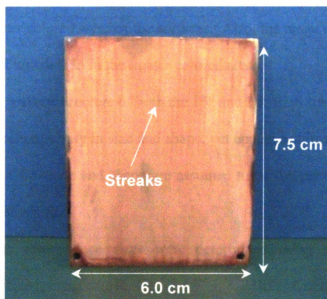


**Figure 3.1.5.** 30° electrochemical deposition surface.

For the 15° EDS the dark streaks are vague and begin to form approximately two-thirds of the way up the plate. The dark streaks on the 30° EDS, however, are very distinct and begin to form approximately halfway up the plate. The difference in appearance of the two surfaces translates into differences in periodic surface structure.

The surface structures of the deposition surfaces were meticulously examined with the ESEM (Figs. 3.1.7 – 3.1.10) and AFM (Figs. 3.1.11-3.1.14). The surface structures are assumed to be closely packed columns formed from the stacking of copper ions. The particle-like surface formations are the visible top faces of the columnar protrusions.

It was found that the variations in mass transfer distribution during deposition resulted in periodic surface structure variations. The dark streaks represent areas in which the surface roughness is slightly greater and the column-faces are slightly larger than that of the lighter colored areas of the surfaces. Also, the range of column-face sizes is greater in the dark streak than in the lighter colored areas.

The general surface structure of both the 15° and 30° EDS resemble that shown in Figure 3.1.6. The columns vary in size and shape, yet appear uniformly distributed. The variations in column-face size and shape are assumed to be the result of “clustering” of copper ions during deposition.

The average column-face sizes were determined using the reference scale provided on the ESEM images (see Fig. 3.1.7 – 3.1.10). Column-face sizes were measured at twenty different locations and were then averaged. The average column-face sizes of the lighter colored areas and dark streaks for the 15° and 30° EDS are given in Table 3.1.2.



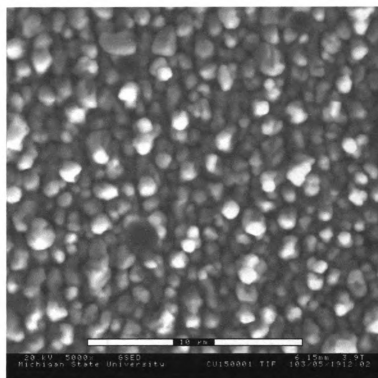


**Figure 3.1.7.** ESEM image of light areas on 15° EDS at 5000x.

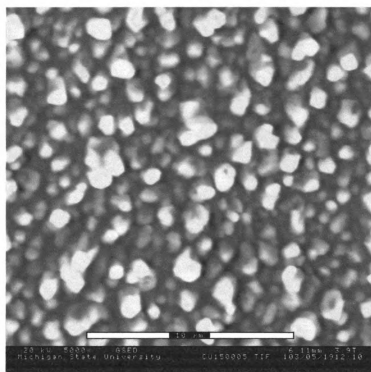


**Figure 3.1.8.** ESEM image of dark streak on 15° EDS at 5000x.

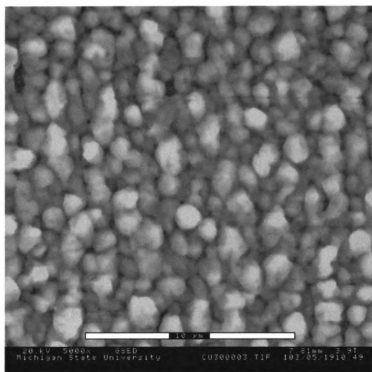


**Figure 3.1.9.** ESEM image of light areas of 30° EDS at 5000x.

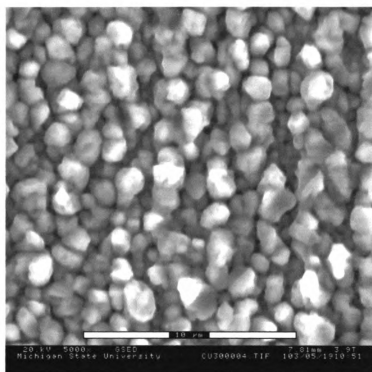


**Figure 3.1.10.** ESEM image of dark streak on 30° EDS at 5000x.

The values of RMS surface roughness, measured with the AFM, were determined for the dark streaks and lighter colored areas of the deposition surfaces. Values are given in nanometers and are given in Table 3.1.3. Again, for a given area, the surface roughness was measured three times and then averaged. Images of the roughness data for both the 15° and 30° surfaces are shown in Figures 3.1.10 – 3.1.13.

The surface roughness of the dark streaks of the 15° and 30° surfaces is approximately 287 nm and is 278% greater than that of the smooth reference surface. For the 15° EDS, the RMS surfaces roughness of the dark streaks is 21% greater than that of the lighter colored areas. For the 30° EDS, The surfaces roughness of the dark streaks is 30% greater than the lighter colored areas. The surface roughness of the lighter areas of the 15° EDS is 8% larger than that of the 30° EDS. Thus the difference in surface roughness between the dark and light areas of the 30° sample is 40% larger than that of the 15° sample.

<i>Area on EDS</i>	<i>RMS Surface Roughness (nm)</i>	
	15°	30°
<i>Light</i>	237	219
<i>Dark Streaks</i>	286	287

**Table 3.1.3.** RMS surface roughness values for 15° and 30° EDS



## Roughness Analysis

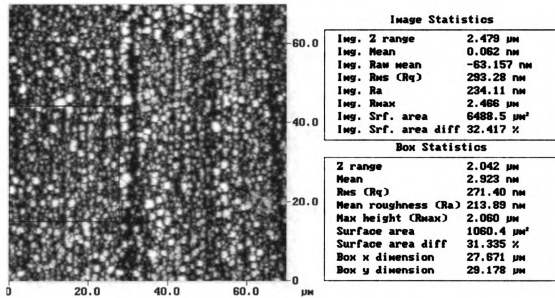


Figure 3.1.11. Surface roughness data for dark streak of 15° EDS

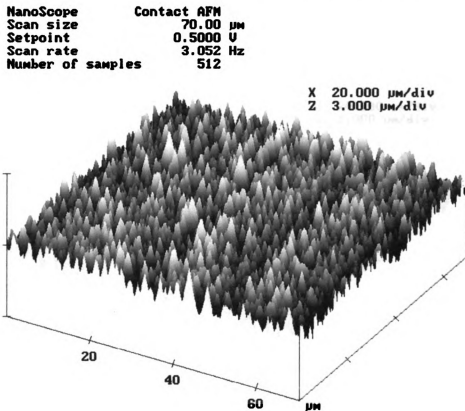


Figure 3.1.12. 3-D surface roughness data for dark streak of 15° EDS.

## Roughness Analysis

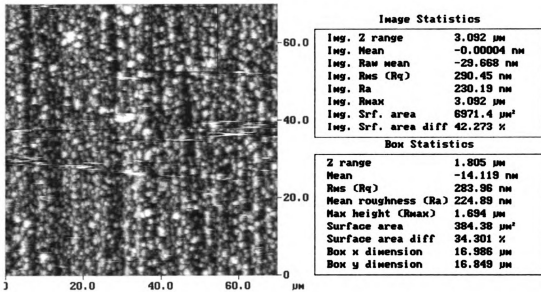


Figure 3.1.13. Surface roughness data for dark streak of 30° EDS

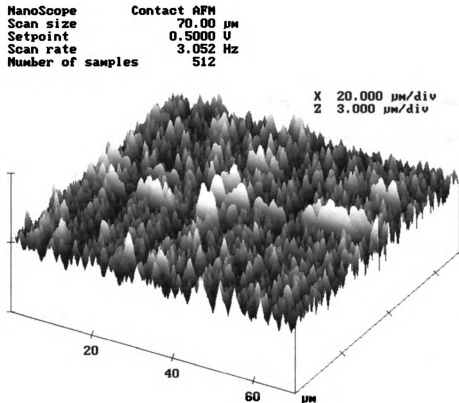


Figure 3.1.14. 3-D surface roughness data for dark streak of 30° EDS.

The AFM also provided maximum height ( $R_{\max}$ ) data for both deposition surfaces. The values of  $R_{\max}$  indicate the difference in height between the highest and lowest points on the surface relative to the mean plane. Image data has a minimum variance about the mean plane of the surface. In other words, the mean plane results from a first-order least-squares fit on the Z data. For the 15° AFM data, the dark streaks and light areas had average  $R_{\max}$  values of 2.9 and 1.9  $\mu\text{m}$  respectively. The 30° EDS had average  $R_{\max}$  values of 2.9 and 1.8  $\mu\text{m}$  for the dark streaks and light areas respectively. For both surfaces, the maximum height difference for the dark streaks and light areas differs by approximately 1  $\mu\text{m}$ .

### **3.2 POOL BOILING**

The experimental pool boiling curves for the smooth, 15°, and 30° surfaces are shown in Figure 3.2.1. Initially, the heat flux increases linearly with increasing wall superheat and is characteristic of natural convection. Once boiling incipience is achieved, the boiling curve is no longer linear. The significant increases in heat flux with increasing wall superheat after boiling incipience verifies that the mode of heat transfer progressed from natural convection to nucleate boiling. The methods used to calculate the surface temperature and heat flux values for the surfaces tested can be found in Appendix D. Experimental boiling data can be found in Appendix E.

The linear portion of the boiling curves indicates that the mode of heat transfer is natural convection. Both the laminar and turbulent natural convection curves for a horizontal upward facing plate are included on Figure 3.2.1. Laminar natural convection

dominates up to a wall superheat of approximately 10 degrees after which turbulent natural convection takes over.

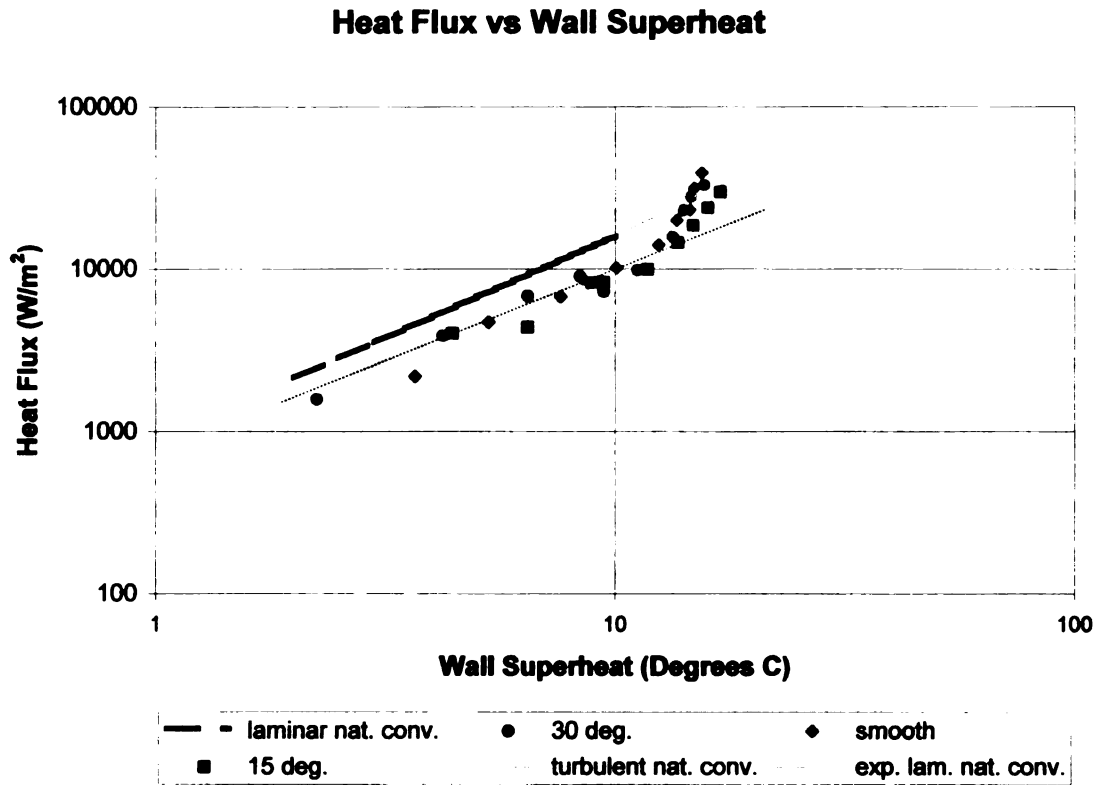


**Figure 3.2.1.** Pool boiling curves for experimental surfaces.

The transition from laminar to turbulent natural convection was determined by the intersection of the two curves. A power-law relationship exists between the non-dimensional Nusselt and Rayleigh numbers resulting in a power-law relationship between heat flux and wall superheat. A power-law curve fit was applied to both the theoretical laminar natural convection curve as well as to the linear portion of the experimental data resulting in curve fit equations of  $q'' = 896 * (\Delta T)^{1.25}$  and  $q'' = 601 * (\Delta T)^{1.2}$  respectively. The exponents on the wall superheat,  $\Delta T$ , differ by a mere 4% thus the theoretical and experimental laminar convection curves are nearly parallel. The experimental laminar

natural convection curve results in heat flux values approximately 20% less than that of the theoretical curve at the same wall superheat. Detailed information for the laminar natural convection calculations can be found in Appendix D.

Thome [32] reported measured the saturated nucleation superheat of water on a plain copper disk at atmospheric pressure to be between 6-8 °C. Boiling incipience, indicated in this work by an initial layer of growing bubbles on the heated surface, occurred at 12-13 °C for the reference smooth surface. This higher value of incipient superheats was anticipated because as the bubbles depart from the heated surface during subcooled boiling, subcooled liquid fills the voids left by the departing bubbles. Thus the filling liquid would take some amount of time to return to saturation conditions.

Boiling incipience on the electrochemical deposition surfaces occurred at 11-12 °C and is only 8% less than that of the reference smooth surface. Microporous enhanced surfaces produced by Chang and You [4] resulted in 80-90% lower superheats compared to a smooth reference surface using FC-72 as the working fluid. Although both of the electrochemical deposition surfaces resulted in a decrease in incipient superheat, this reduction is minimal within the uncertainty of this work. This reduction in incipient superheat will not be used to indicate whether or not the electrochemical deposition surfaces can be considered enhanced boiling surfaces.

The portion of the boiling curves after boiling incipience for the smooth, 15° EDS and 30° EDS are very similar (see Fig. 3.2.1). The data for the 30° porous electrochemical deposition surface virtually collapses onto the smooth surface data. For the boiling on the 15° EDS, the heat flux for a given wall superheat is slightly less than that of the 30° EDS and smooth surface data.

Bubble visualization was also used to evaluate boiling on the different surfaces tested. Still images of bubble growth on each surface were captured from digital video recordings of boiling incipience. Figures 3.3.2 – 3.3.4 represent bubble growth on the surfaces tested at boiling incipience and are shown at equal length scales.

As discussed previously, a surface can enhance boiling by either reducing the incipient superheat (increasing the effective heat transfer coefficient) or increasing the nucleation site density at incipience as compared to a smooth surface. From Figures 3.2.2 and 3.2.3, it is obvious that the 30° EDS promotes bubble growth and increases the nucleation site density compared to the smooth reference surface. This increase in nucleation site density implies that the 30° surface can be considered an enhanced boiling heat transfer surface. Bubbles on the 30° surface, as shown in Figure 3.2.3, appear to form uniformly in periodic clusters across the boiling surface. This suggests that the periodic surface structure variations on this surface promote preferred nucleation sites. Bubble formation on the 15° EDS (Fig. 3.2.4) also depicts periodic clusters, however, there is not an increase in the nucleation site density at boiling inception as compared to the smooth surface. This lack of bubble formation on the 15° surface is responsible for the lower heat flux for a given wall superheat as compared to the smooth and 30° surfaces. Boiling inception on the 30° surface produced a significantly greater nucleation site density than that on the 15° surface. This suggests that the more pronounced surface structure of the 30° surface, compared to the less distinct structure of the 15° surface, increases nucleation site density at boiling inception.

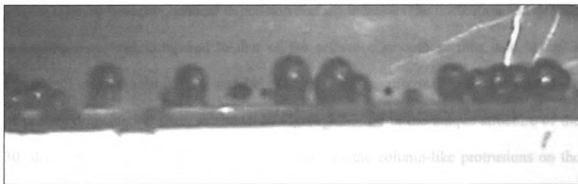


**Figure 3.2.2.** Bubble formation on smooth reference surface.

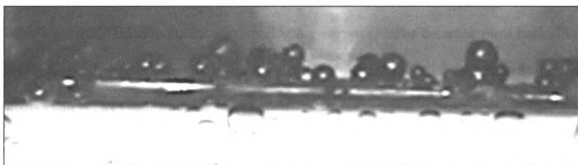


**Figure 3.2.3.** Bubble formation on 30° electrochemical deposition surface.



**Figure 3.2.4.** Bubble formation on 15° electrochemical deposition surface.

The 30 ° electrochemical deposition surface increases the nucleation site density at boiling inception, compared to that of the reference smooth surface, and hence is considered an enhanced boiling surface. The mechanisms responsible for the promotion of preferred nucleation sites, as shown in Figure 3.2.3, lie in the unique structure of the 30° deposition surface. The packing distribution of the column-like protrusions on the surface appears to create vapor-trapping pockets. These pockets can then act as steam evacuation channels and become preferred sites for the formation of smaller bubbles. The height distribution of the columns also creates a mechanism for preferred sites of bubble growth. Taller columns surrounding a group of smaller columns form basin-like areas in which larger vapor bubbles could grow. Also, on a slightly larger scale, the streaks can act as vapor trapping mechanisms.

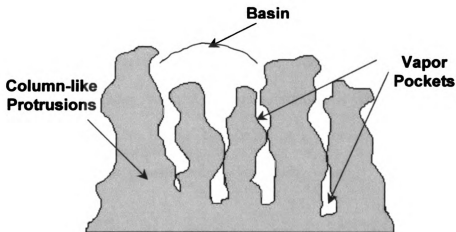


**Figure 3.2.5.** Magnified schematic of possible vapor pockets on deposition surface.



The streaks, as previously stated, consist of periodic spanwise surface variations that extend longitudinally along the plate. These unique variations can be thought of as troughs (Fig. 3.2.6) which trap vapor in the same manner as basins. The troughs simply are basins on a larger scale that extend into the page.

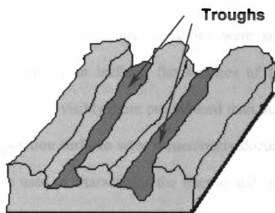


**Figure 3.2.6.** Magnified schematic of possible troughs on deposition surface.

## **CHAPTER 4**

### **CONCLUSIONS**

The following summary and resulting conclusions are supported by the experimental work performed in this investigation. Micro-scale structured copper surfaces with periodic surface structure variations were successfully created using electrochemical deposition on an inclined flat surfaces of 15° and 30°. The surface structure of the 30° surface is visibly more pronounced than that of the 15° surface. The structures of these deposition surfaces were meticulously documented in this work. The ESEM and AFM were used to characterize the micron and sub-micron sized structural features of the surfaces. Boiling incipience on the deposition surfaces was investigated and compared to that of a smooth reference surfaces. Boiling evaluation of the smooth, 15° and 30° surfaces suggests that the more distinct structure of the 30° surface increases the nucleation site density at boiling inception. These preferred nucleation sites are formed by: vapor-trapping pockets between column-like protrusions present on the surface; basins created by height differences in clusters of columns; and troughs characterized by spanwise periodic column variations.

## **CHAPTER 5**

### **RECOMMENDATIONS**

Suggestions for future work in the area of nucleate pool boiling on microscale structured electrochemical deposition surfaces are as follows:

1. Use low surface tension working fluid
2. Measure the contact angles on both the light areas and dark streaks of the electrochemical deposition surfaces. This could help quantify the effects of the differences in surface structure of the EDS.
3. Design an experimental set-up for top-view bubble visualization. If a visual recording device was used to document bubble growth on the entire electrochemical deposition surface, preferred nucleation sites could be directly related to particle composition and surface structure.
4. Include the presence of an electric field in the experimental set-up. The results of the electric field boiling data could help further characterize the electrochemical deposition surfaces.

## **APPENDICES**

## APPENDIX A

### STEADY-STATE VERIFICATION

**PURPOSE:** This experiment was designed for testing the assumption that, after raising the supplying energy level to the test section, 15 minutes is enough for time for the temperature to reach the steady state.

**PROCEDURE:** Once the liquid was heated to 90 degree Celsius (10 degree subcooling), the power to the heater cartridges was increased in increments of 5 on the Vatic every 30 minutes. Special care is taken to keep the liquid temperature at 90 degree Celsius. Temperature data for Channel 8 shown on the Omega Trendicator is taken every 2 minutes.

**DATA:**

Voltage(V)	Time (min)	Temp. for Ch. 8
20V	1	89.8
	3	89.8
	5	90
	7	90.4
	9	90.5
	11	90.4
	13	90.6
	15	90.6
	17	90.6
	19	90.4
	21	90.5
	23	90.5
	25	90.4
	27	90.7
	29	90.5

Voltage(V)	Time (min)	Temp. for Ch. 8
25V	31	90.7
	33	90.9
	35	91.2
	37	91.5
	39	91.8
	41	92.2
	43	92.1
	45	92.2
	47	92.2
	49	92.2
	51	91.2
	53	92.2
	55	92.2
	57	92.2
	59	92.2

<b>Voltage(V)</b>	<b>Time (min)</b>	<b>Temp. for Ch. 8</b>
<b>30V</b>	61	93.3
	63	93.9
	65	94.3
	67	94.2
	69	94.2
	71	94.3
	73	94.3
	75	94.3
	77	94.4
	79	94.2
	81	94.3
	83	94.5
	85	94.3
	87	94.3
	89	94.2

<b>Voltage(V)</b>	<b>Time (min)</b>	<b>Temp. for Ch. 8</b>
<b>35V</b>	91	95.3
	93	96.5
	95	96.9
	97	96.8
	99	96.9
	101	96.9
	103	97
	105	97
	107	97
	109	96.9
	111	96.5
	113	96.8
	115	97
	117	97.1
	119	97.2

<b>Voltage(V)</b>	<b>Time (min)</b>	<b>Temp. for Ch. 8</b>
<b>40V</b>	120	97.9
	122	98.3
	124	98.5
	126	98.5
	128	98.6
	130	98.7
	132	98.9
	134	98.7
	136	98.6
	138	98.6
	140	98.7
	142	98.8
	144	98.8
	146	98.9
	148	98.8

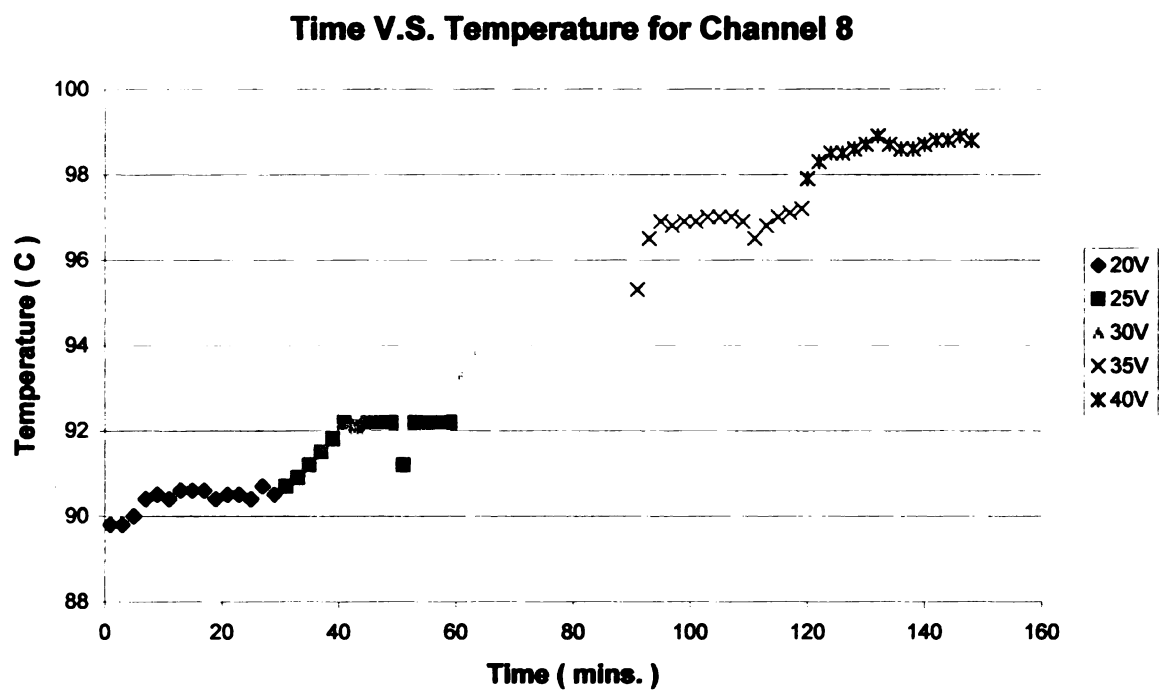


**Figure A1.** Time V.S. temperature for Channel 8 while changing Variac setting.

## APPENDIX B

### DETERMINATION OF PHYSICAL PROPERTIES

The determination of the physical properties of the electrolyte solution was accomplished by the following method used by Lloyd [28].

#### Density of Electrolyte Solution

The equation for the density of the copper ion-sulfuric acid solution, as shown below, was a least squares curve fitted to through a plot of density as a function of copper ion and sulfuric acid concentration and of temperature.

$$\rho = AH(T) + BH(T) \cdot HS + CH(T) \cdot HS^2 + DH(T) \cdot CU + EH(T) \cdot CU^2$$

In the above equation, HS and CU are the molar sulfuric acid and copper ion concentrations respectively and

$$AH(T) = 1.0060 - (0.000006 \cdot T) - (0.0000052 \cdot T^2)$$

$$BH(T) = 0.06735 - (0.00033 \cdot T) + (0.00000317 \cdot T^2)$$

$$CH(T) = -0.00341 + (0.000041 \cdot T) - (0.00000048 \cdot T^2)$$

$$DH(T) = 0.12717 + (0.000307 \cdot T) - (0.0000177 \cdot T^2)$$

$$EH(T) = 0.03225 - (0.00144 \cdot T) + (0.00004053 \cdot T^2)$$

where T is the solution temperature in degrees Centigrade.

#### Viscosity of Electrolyte Solution

The equation for the viscosity of the copper ion-sulfuric acid solution, as shown below, was a least squares curve fitted to through a plot of viscosity as a function of copper ion and sulfuric acid concentration and of temperature.

$$\mu = AV(T) + BV(T) \cdot HS + CV(T) \cdot HS^2 + DV(T) \cdot CU + EV(T) \cdot CU^2$$



In the above equation, the coefficients of sulfuric and copper ion concentrations are

$$AV(T) = 1.69713 - (0.045652 \cdot T) + (0.000535 \cdot T^2)$$

$$BV(T) = 0.330104 - (0.008309 \cdot T) + (0.000072 \cdot T^2)$$

$$CV(T) = 0.01317133 - (0.00037356 \cdot T) + (0.00000763 \cdot T^2)$$

$$DV(T) = 2.3982 - (0.13872 \cdot T) + (0.002267 \cdot T^2)$$

$$EV(T) = 0.99679 + (0.14558 \cdot T) - (0.0032494 \cdot T^2)$$

### Diffusion Coefficients

The least squares best-fit equation for the diffusion coefficient for the sulfuric acid is

$$D_{HS} = (AK(T) + BK(T) \cdot HS + CK(T) \cdot HS^{0.5}) \cdot 10^{-5}$$

where

$$AK(T) = 0.92452 + (0.042135 \cdot T) + 0.00005207 \cdot T^2$$

$$BK(T) = 0.061912 - (0.001293 \cdot T) - (0.00024615 \cdot T^2)$$

$$CK(T) = 0.6688 - (0.004727 \cdot T) + (0.0004895 \cdot T^2)$$

At 22°C the copper ion concentration is

$$D_{CU} = \frac{(0.7363 + (0.00511 \cdot HS) + (0.02044 \cdot CU)) \cdot 10^{-5}}{\mu}$$

### Transference Numbers

The expression used in this work for the transference numbers of copper ions and hydrogen ions are as follows

$$t_{cu^{++}} = (0.2633 - (0.102 \cdot HS)) \cdot CU$$

$$t_H = 0.8156 - (0.2599 \cdot CU) - (0.1089 \cdot CU^2)$$

## APPENDIX C

### CALCULATION OF PHYSICAL PROPERTIES

#### 15 Degrees

##### Density of Electrolyte Solution

Temperaure (degrees C)	22.6000
CH (molar conc. H <sub>2</sub> SO <sub>4</sub> )	1.5000
CU (molar conc. CuSO <sub>4</sub> )	0.03
AH	1.0032
BH	0.0615
DH	-0.0027
PH	0.1276
RH	0.0308
<b>Total Density (g/cm<sup>3</sup>)</b>	<b>1.093</b>
<b>Density w/out CuSO<sub>4</sub> (g/cm<sup>3</sup>)</b>	<b>1.089</b>
<b>Density Change (g/cm<sup>3</sup>)</b>	<b>0.004</b>

##### Viscosity of Electrolyte Solution

AV	0.9386514
BV	0.17909532
CV	0.0086
DV	0.4210
EV	2.6272
Total Viscosity	1.2417
<b>Correct Viscosity (g/(cm*s))</b>	<b>0.0124</b>

##### Diffusion Coefficients

AK	1.9034
BK	0.4642
DK	0.811987
<b>Diff. Coeff. H<sub>2</sub>SO<sub>4</sub> (cm<sup>2</sup>/s)</b>	<b>0.0000359</b>
<b>Diff. Coeff. CuSO<sub>4</sub> (cm<sup>2</sup>/s)</b>	<b>0.0000060</b>

##### Transference Numbers

t-CuSO <sub>4</sub>	0.0033
t-H <sub>2</sub> SO <sub>4</sub>	0.8077

**Miscellaneous Values**

theta (degrees)	15.0000
theta (rad)	0.2617
gravity (m/s^2)	981.0000
cos theta	0.9660
x-location (cm)	7.5000000

**Mass Transfer Coefficient**

current density (A/cm^2)	0.1660000
CU conc. (g/cm^3)	0.00478860
n	2
F ((A*s)/g)	96500
Km (cm/s)	<b>0.00017902</b>

Schmidt #	1894.1983
Grashof #	10928358.0695
Rayleigh #	20700477202.0999
Sherwood #	223.9080
Sh(Ra)#	189.2760

**30 Degrees****Density of Electrolyte Solution**

Temperaure (degrees C)	24.0000
CH (molar conc. H2SO4)	1.5000
CU (molar conc. CuSO4)	0.03
AH	1.0029
BH	0.0613
DH	-0.0027
PH	0.1276
RH	0.0308
Total Density (g/cm^3)	<b>1.093</b>
Density w/out CuSO4 (g/cm^3)	<b>1.089</b>
Density Change (g/cm^3)	<b>0.004</b>

**Viscosity of Electrolyte Solution**

AV	0.909642
BV	0.17216
CV	0.0086

DV	0.3747
EV	2.6191
Total Viscosity	1.2008
<b>Correct Viscosity (g/(cm*s))</b>	<b>0.0120</b>

#### **Diffusion Coefficients**

AK	1.9658
BK	0.4463
DK	0.837304
<b>Diff. Coeff. H2SO4 (cm^2/s)</b>	<b>0.0000366</b>
<b>Diff. Coeff. CuSO4 (cm^2/s)</b>	<b>0.0000062</b>

#### **Transference Numbers**

t-CuSO4	0.0033
t-H2SO4	0.8077

#### **Miscellaneous Values**

theta (degrees)	30.0000
theta (rad)	0.5233
gravity (m/s^2)	981.0000
cos theta	0.8662
x-location (cm)	7.5000000

#### **Mass Transfer Coefficient**

current density (A/cm^2)	0.1660000
CU conc. (g/cm^3)	0.00478860
n	2
F ((A*s)/g)	96500
<b>Km (cm/s)</b>	<b>0.00017902</b>

<b>Schmidt #</b>	<b>1772.6587</b>
<b>Grashof #</b>	<b>10471122.0308</b>
<b>Rayleigh #</b>	<b>18561725884.3779</b>
<b>Sherwood #</b>	<b>216.5390</b>
<b>Sh(Ra)#</b>	<b>184.1854</b>

## APPENDIX D

### POOL BOILING CALCULATIONS

#### C.1 HEAT FLUX

The heat flux through the boiling surface was determined using Fourier's Law:

$$q'' = -k \frac{dT}{dx} \quad \text{C.1.1}$$

where  $k$  is the known thermal conductivity of the boiling surface and  $dT/dx$  is the average temperature gradient through the OFHC copper block. The average temperature gradient through the OFHC copper block is determined by averaging three measured x-location temperature gradients. An x-location temperature gradient profile is determined by plotting the known y-location of a thermocouple versus its temperature display for four consecutive thermocouples. Plots are generated for three sets of thermocouples: #1-4, #5-8, and #9-12 for each variac setting for each surface (see Appendix E).

#### C.2 SURFACE TEMPERATURE

For conduction through a series of materials, the thermal resistance model for the heat flux through a wall is equal to

$$q'' = \frac{T_0 - T_w}{R_{tot}} \quad \text{C.2.1}$$

where  $q''$  is the heat flux through the surface,  $T_0$  is a known temperature in the material and  $T_w$  is the surface temperature of the material.  $R_{tot}$  is the total thermal resistance through the material. Solving the thermal resistance model for equation for  $T_w$  gives:

$$T_w = T_0 - q'' \cdot R_{tot} \quad \text{C.2.2}$$

where, for this work,  $q''$  is the measured value of the heat flux through the boiling surface,  $T_0$  is the average of five thermocouple readings at a known location in the OFHC copper block, and  $T_w$  is the unknown temperature of the boiling surface.  $R_{tot}$  is equal to the sum of the resistances for each material as shown below.

$$R_{tot} = R_1 + R_2 + R_3 \quad \text{C.2.3}$$

where  $R_1$  is the thermal resistance of the OFHC copper block,  $R_2$  is the thermal resistance of the solder layer, and  $R_3$  is the thermal resistance of the boiling surface as defined below.

$$R_1 = \frac{L_1}{k_1} \quad \text{C.2.4}$$

$$R_2 = \frac{L_2}{k_2} \quad \text{C.2.5}$$

$$R_3 = \frac{L_3}{k_3} \quad \text{C.2.6}$$

For the resistances defined above,  $L$  is equal to the known thickness of the material and  $k$  is the known thermal conductivity of the material. Note that  $L_1$  is the distance from the known temperature of the OFHC copper,  $T_0$ , to the solder layer. The table shown below gives the length and thermal conductivity values used to calculate the total thermal resistance.

	1	2	3
	OFHC	Solder	110 Alloy
<b>k (W/mK)</b>	391	50	388
<b>L (m)</b>	0.002	0.0005	0.001
<b>R (m<sup>2</sup>K/W)</b>	5.12 E-06	0.00001	2.58 E-06
<b>R-tot (m<sup>2</sup>K/W)</b>	1.77 E-05		

**Table C.2.1** Values used for thermal resistance model.

### C.3 HEAT TRANSFER COEFFICIENT

The boiling heat transfer coefficient was calculated using the following equation:

$$h = \frac{q''}{(T_w - T_{sub})} \quad \text{C.3.1}$$

where  $q''$  is the heat flux through the boiling surface,  $T_w$  is the temperature of the boiling surface, and  $T_{sub}$  is the temperature of the subcooled liquid.

### C.4 NATURAL CONVECTION CURVES

The heat flux versus temperature values for the natural convection curves were calculated using the following series of equations. Heat flux can be defined as

$$q'' = h \cdot (T_w - T_{sub}) \quad \text{C.4.1}$$

where  $h$  is the convective heat transfer coefficient and is calculated by

$$h = \frac{k}{\delta} \cdot Nu \quad \text{C.4.2}$$

In the above equation,  $k$  is the thermal conductivity of the liquid,  $\delta$  is the characteristic length of the heat transfer surface equal to its area divided by perimeter, and  $Nu$  is the Nusselt number. The Nusselt number for laminar flow and turbulent flow are defined as

$$\text{Laminar:} \quad Nu = 0.54 \cdot Ra^{1/4} \quad (10^4 \leq Ra \leq 10^7) \quad \text{C.4.3}$$

$$\text{Turbulent:} \quad Nu = 0.15 \cdot Ra^{1/3} \quad (10^7 \leq Ra \leq 10^{11}) \quad \text{C.4.4}$$

where  $Ra$  is the Rayleigh number. The Rayleigh number can be calculated using known properties of the liquid with the following equation:

$$Ra = \frac{g \cdot \beta \cdot (T_w - T_{sub}) \cdot \delta^3 \cdot Pr}{\nu^2} \quad \text{C.4.5}$$

For this work, the Rayleigh numbers were less than  $10^7$  thus the laminar equation for the Nusselt could be used. Table C.4.1 defines and give the values for the variables in the above equation.

Parameter	Symbol	Units	Value
Specific Heat (liq.)	$C_p$	J/(kg°C)	4217
Thermal Diffusivity (liq.)	$\alpha$	m <sup>2</sup> /s	1.68 E-07
Thermal Conductivity (liq.)	$k$	W/(m*K)	0.679
Surface Area	$A$	m <sup>2</sup>	0.0019
Surface Perimeter	$P$	m	0.178
Characteristic Length (A/P)	$\delta$	m	0.0111
Prandtl Number	$Pr$	none	1.75
Acceleration due to gravity	$g$	m/s <sup>2</sup>	9.81
Beta	$\beta$	1/K	0.002
Dynamic Viscosity (liq.)	$\mu_l$	kg/(m*s)	0.00028
Density (liq.)	$\rho_l$	kg/m <sup>3</sup>	957
Kinematic Viscosity (u/p)	$\nu$	m <sup>2</sup> /s	2.95 E-07
Density (vapor)	$\rho_v$	kg/m <sup>3</sup>	0.6
Surface Tension	$\sigma$	N/m	0.0589
Enthalpy of Vaporization	$h_{fg}$	J/kg	2257000
Experimentall Boiling Constant	$C_{sf}$	none	0.013

**Table C.4.1** Property values for variables used in boiling data calculations.



## APPENDIX E

### POOL BOILING DATA

Surface	Wall Superheat (deg C)	Heat Flux (W/m <sup>2</sup> )	Heat Transfer Coefficient (W/m <sup>2</sup> K)	Variac Setting
Smooth	3.67	2173.96	592.11	15
	5.31	4700.21	885.69	20
	7.61	6732.24	884.55	25
	8.53	8682.16	1018.27	30
	10.06	10139.41	1007.83	35
	12.44	14039.25	1128.41	40
	<b>13.64*</b>	19888.61	1458.31	45
	14.57	23049.45	1581.74	50
	14.87	31464.55	2115.50	55
	15.44	38853.67	2516.01	60
15 Degree	2.24	1573.38	701.73	15
	4.22	3879.23	918.95	20
	6.45	6793.63	1053.31	25
	8.39	9030.93	1076.36	30
	9.44	7224.90	765.17	35
	<b>11.18*</b>	9852.03	881.56	40
	13.32	15701.39	1178.59	45
	14.12	22947.01	1624.68	50
	14.64	27729.33	1894.16	55
	15.65	32819.37	2097.17	60
30 Degree	4.43	4002.28	903.61	20
	6.45	4371.77	677.52	25
	8.90	8209.83	921.96	30
	9.43	8271.61	876.82	35
	<b>11.75*</b>	9913.41	843.36	40
	13.70	14490.46	1057.42	45
	14.79	18513.46	1251.55	50
	15.89	23829.50	1499.80	55
	16.93	29556.08	1746.08	60

\* indicates boiling incipience

Smooth

### THERMOCOUPLE LOCATIONS

#4	#13	#8	#14	#12
#3		#7		#11
#2		#6		#10
#1		#5		#9

Y-Direction (m)	15	X-Direction (m)					Average
		0.009525	0.015875	0.022225	0.028575	0.034925	
	0.022225	93.45	93.6	93.45	93.45	93.6	
	0.015875	93.5		93.5		93.6	
	0.009525	93.5		93.55		93.65	
	0.003175	93.55		93.6		93.7	
	dT/dx [slope]	-4.72		-9.45		-5.51	<b>-5.56</b>
	dT/dx ave.	-5.56					
	q" ave. (w/m^2)	2173.96					
	To ave. (degree C)	93.51					
	Tw (degree C)	93.472					
	T bulk (degree C)		89.900		89.700		
	T bulk ave. (deg C)	89.800					
	h exp. (W/m^2K)	592.112					

20	0.009525	0.015875	0.022225	0.028575	0.034925	Average
0.022225	95.95	96	96	95.9	96.1	95.99
0.015875	96		96.05		96.1	96.05
0.009525	96.05		96.15		96.2	96.13
0.003175	96.15		96.2		96.3	96.22
dT/dx [slope]	-7.87		-15.75		-11.81	<b>-12.021</b>
dT/dx ave.	-12.021					
q" ave. (w/m^2K)	4700.211					
To ave. (degree C)	95.99					
Tw (degree C)	95.907					
T bulk (degree C)		90.400		90.800		
T bulk ave. (deg C)	90.600					
h exp. (W/m^2K)	885.689					

25	0.009525	0.015875	0.022225	0.028575	0.034925	Average
0.022225	98.25	98.35	98.25	98.15	98.4	98.28
0.015875	98.3		98.35		98.55	98.40

0.009525	98.45		98.45		98.55	98.48
0.003175	98.5		98.6		98.75	98.62
dT/dx [slope]	-15.748		-20.472		-19.67	<b>-17.218</b>
dT/dx ave.	-17.218					
q" ave. (w/m^2K)	6732.238					
To ave. (degree C)	98.28					
Tw (degree C)	98.161					
T bulk (degree C)		90.300		90.800		
T bulk ave. (deg C)	90.550					
h exp. (W/m^2K)	884.553					

<b>30</b>	0.009525	0.015875	0.022225	0.028575	0.034925	<b>Average</b>
0.022225	99.4	99.45	99.35	99.25	99.45	99.38
0.015875	99.45		99.45		99.55	99.48
0.009525	99.55		99.55		99.65	99.58
0.003175	99.75		99.8		99.9	99.82
dT/dx [slope]	-20.472		-26.772		-22.047	<b>-22.205</b>
dT/dx ave.	-22.205					
q" ave. (w/m^2K)	8682.155					
To ave. (degree C)	99.38					
Tw (degree C)	99.226					
T bulk (degree C)		90.600		90.800		
T bulk ave. (deg C)	90.700					
h exp. (W/m^2K)	1018.268					

<b>35</b>	0.009525	0.015875	0.022225	0.028575	0.034925	<b>Average</b>
0.022225	100.95	101.1	100.85	101	101.05	100.99
0.015875	101.05		101.05		101.05	101.05
0.009525	101.25		101.2		101.35	101.27
0.003175	101.4		101.4		101.6	101.47
dT/dx [slope]	-15.75		-20.472		-26.77	<b>-25.932</b>
dT/dx ave.	-25.932					
q" ave. (w/m^2K)	10139.412					
To ave. (degree C)	100.99					
Tw (degree C)	100.811					
T bulk (degree C)		90.600		90.900		
T bulk ave. (deg C)	90.750					
h exp. (W/m^2K)	1007.833					

<b>40</b>	0.009525	0.015875	0.022225	0.028575	0.034925	<b>Average</b>
0.022225	103.4	103.6	103.3	103.3	103.6	103.44
0.015875	103.45		103.6		103.65	103.57

0.009525	103.75		103.8		104.05	103.87
0.003175	103.95		104.1		104.25	104.10
dT/dx [slope]	-22.05		-33.071		-29.92	<b>-35.906</b>
dT/dx ave.	-35.906					
q" ave. (w/m^2K)	14039.246					
To ave. (degree C)	103.44					
Tw (degree C)	103.192					
T bulk (degree C)		90.600		90.900		
T bulk ave. (deg C)	90.750					
h exp. (W/m^2K)	1128.411					

<b>45</b>	0.009525	0.015875	0.022225	0.028575	0.034925	<b>Average</b>
0.022225	104.75	104.75	104.65	104.5	104.8	104.69
0.015875	104.85		105.05		104.9	104.93
0.009525	105.25		105.25		105.35	105.28
0.003175	105.55		105.65		105.75	105.65
dT/dx [slope]	-32.28		-44.09		-44.09	<b>-50.866</b>
dT/dx ave.	-50.866					
q" ave. (w/m^2K)	19888.606					
To ave. (degree C)	104.69					
Tw (degree C)	104.338					
T bulk (degree C)		90.600		90.800		
T bulk ave. (deg C)	90.700					
h exp. (W/m^2K)	1458.310					

<b>50</b>	0.009525	0.015875	0.022225	0.028575	0.034925	<b>Average</b>
0.022225	105.6	105.75	105.5	105.6	105.7	105.63
0.015875	105.75		105.95		105.85	105.85
0.009525	106.15		106.25		106.45	106.28
0.003175	106.65		106.7		106.85	106.73
dT/dx [slope]	-42.52		-66.142		-64.567	<b>-58.95</b>
dT/dx ave.	-58.95					
q" ave. (w/m^2K)	23049.45					
To ave. (degree C)	105.63					
Tw (degree C)	105.222					
T bulk (degree C)		90.500		90.800		
T bulk ave. (deg C)	90.650					
h exp. (W/m^2K)	1581.741					

<b>55</b>	0.009525	0.015875	0.022225	0.028575	0.034925	<b>Average</b>
0.022225	106.4	106.5	106.3	106.3	106.4	106.38
0.015875	106.6		106.7		106.7	106.67

0.009525	107.2		107.25		107.5	107.32
0.003175	107.7		107.9		108	107.87
dT/dx [slope]	-57.48		-66.142		-72.441	<b>-80.472</b>
dT/dx ave.	-80.472					
q" ave. (w/m^2K)	31464.552					
To ave. (degree C)	106.38					
Tw (degree C)	105.823					
T bulk (degree C)		90.900		91.000		
T bulk ave. (deg C)	90.950					
h exp. (W/m^2K)	2115.503					

<b>60</b>	0.009525	0.015875	0.022225	0.028575	0.034925	<b>Average</b>
0.022225	107.1	107.2	106.9	106.9	107.3	107.08
0.015875	107.45		107.7		107.5	107.55
0.009525	108.05		108.25		108.45	108.25
0.003175	108.8		108.95		109.1	108.95
dT/dx [slope]	-63.78		-91.34		-83.465	<b>-99.37</b>
dT/dx ave.	-99.37					
q" ave. (w/m^2K)	38853.67					
To ave. (degree C)	107.08					
Tw (degree C)	106.393					
T bulk (degree C)		90.800		91.100		
T bulk ave. (deg C)	90.950					
h exp. (W/m^2K)	2516.008					

**15 Degrees**

#### **THERMOCOUPLE LOCATIONS**

<b>#4</b>	<b>#13</b>	<b>#8</b>	<b>#14</b>	<b>#12</b>
<b>#3</b>		<b>#7</b>		<b>#11</b>
<b>#2</b>		<b>#6</b>		<b>#10</b>
<b>#1</b>		<b>#5</b>		<b>#9</b>

<b>Y-Direction (m)</b>	<b>15</b>	<b>X-Direction (m)</b>					
		0.009525	0.015875	0.022225	0.028575	0.034925	<b>Average</b>
	0.022225	93.4	93.6	93.5	93.5	93.6	93.52
	0.015875	93.4		93.5		93.6	93.50
	0.009525	93.4		93.5		93.6	93.50
	0.003175	93.45		93.5		93.7	93.55
	dT/dx [slope]	-4.72		-9.45		-5.51	<b>-1.417</b>
	dT/dx ave.	-1.417					

q" ave. (w/m^2)	554.047			
To ave. (degree C)	93.52			
Tw (degree C)	93.510			
T bulk (degree C)	89.900		89.700	
T bulk ave. (deg C)	89.800			
h exp. (W/m^2K)	149.331			

<b>20</b>	0.009525	0.015875	0.022225	0.028575	0.034925	<b>Average</b>
0.022225	95	95.2	95.1	95	95.2	95.10
0.015875	95		95.1		95.2	95.10
0.009525	95.1		95.1		95.4	95.20
0.003175	95.2		95.2		95.45	95.28
dT/dx [slope]	-7.87		-15.75		-11.81	<b>-10.236</b>
dT/dx ave.	-10.236					
q" ave. (w/m^2K)	4002.276					
To ave. (degree C)	95.1					
Tw (degree C)	95.029					
T bulk (degree C)	90.400		90.800			
T bulk ave. (deg C)	90.600					
h exp. (W/m^2K)	903.614					

<b>25</b>	0.009525	0.015875	0.022225	0.028575	0.034925	<b>Average</b>
0.022225	96.9	97.2	97.1	97	97.2	97.08
0.015875	96.9		97.1		97.2	97.07
0.009525	97		97.1		97.4	97.17
0.003175	97.15		97.2		97.5	97.28
dT/dx [slope]	-15.748		-20.472		-19.67	<b>-11.181</b>
dT/dx ave.	-11.181					
q" ave. (w/m^2K)	4371.771					
To ave. (degree C)	97.08					
Tw (degree C)	97.003					
T bulk (degree C)	90.300		90.800			
T bulk ave. (deg C)	90.550					
h exp. (W/m^2K)	677.515					

<b>30</b>	0.009525	0.015875	0.022225	0.028575	0.034925	<b>Average</b>
0.022225	99.6	99.85	99.75	99.55	100	99.75
0.015875	99.6		99.8		100	99.80
0.009525	99.8		99.85		100.15	99.93
0.003175	100		100.1		100.35	100.15
dT/dx [slope]	-20.472		-26.772		-22.047	<b>-20.997</b>
dT/dx ave.	-20.997					

q" ave. (w/m^2K)	8209.827			
To ave. (degree C)	99.75			
Tw (degree C)	99.605			
T bulk (degree C)	90.600		90.800	
T bulk ave. (deg C)	90.700			
h exp. (W/m^2K)	921.961			

<b>35</b>	0.009525	0.015875	0.022225	0.028575	0.034925	<b>Average</b>
0.022225	100.2	100.45	100.3	100.15	100.55	100.33
0.015875	100.2		100.45		100.55	100.40
0.009525	100.35		100.5		100.75	100.53
0.003175	100.6		100.7		100.9	100.73
dT/dx [slope]	-15.75		-20.472		-26.77	<b>-21.155</b>
dT/dx ave.	-21.155					
q" ave. (w/m^2K)	8271.605					
To ave. (degree C)	100.33					
Tw (degree C)	100.184					
T bulk (degree C)	90.600			90.900		
T bulk ave. (deg C)	90.750					
h exp. (W/m^2K)	876.819					

<b>40</b>	0.009525	0.015875	0.022225	0.028575	0.034925	<b>Average</b>
0.022225	102.65	102.85	102.55	102.45	102.9	102.68
0.015875	102.65		102.85		102.9	102.80
0.009525	102.8		102.9		103.15	102.95
0.003175	103.05		103.1		103.35	103.17
dT/dx [slope]	-22.05		-33.071		-29.92	<b>-25.354</b>
dT/dx ave.	-25.354					
q" ave. (w/m^2K)	9913.414					
To ave. (degree C)	102.68					
Tw (degree C)	102.505					
T bulk (degree C)	90.600			90.900		
T bulk ave. (deg C)	90.750					
h exp. (W/m^2K)	843.364					

<b>45</b>	0.009525	0.015875	0.022225	0.028575	0.034925	<b>Average</b>
0.022225	104.75	104.8	104.5	104.35	104.9	104.66
0.015875	104.75		105		105.45	105.07
0.009525	104.95		105.15		105.35	105.15
0.003175	105.35		105.35		105.55	105.42
dT/dx [slope]	-32.28		-44.09		-44.09	<b>-37.06</b>
dT/dx ave.	-37.06					

q" ave. (w/m^2K)	14490.46				
To ave. (degree C)	104.66				
Tw (degree C)	104.404				
T bulk (degree C)	90.600		90.800		
T bulk ave. (deg C)	90.700				
h exp. (W/m^2K)	1057.418				

<b>50</b>	0.009525	0.015875	0.022225	0.028575	0.034925	<b>Average</b>
0.022225	105.85	105.95	105.55	105.45	106.05	105.77
0.015875	105.85		106.1		106.1	106.02
0.009525	106.15		106.3		106.55	106.33
0.003175	106.55		106.6		106.85	106.67
dT/dx [slope]	-42.52		-66.142		-64.567	<b>-47.349</b>
dT/dx ave.	-47.349					
q" ave. (w/m^2K)	18513.459					
To ave. (degree C)	105.77					
Tw (degree C)	105.442					
T bulk (degree C)	90.500		90.800			
T bulk ave. (deg C)	90.650					
h exp. (W/m^2K)	1251.548					

<b>55</b>	0.009525	0.015875	0.022225	0.028575	0.034925	<b>Average</b>
0.022225	107.45	107.45	107	106.85	107.55	107.26
0.015875	107.45		107.65		107.75	107.62
0.009525	107.75		107.95		108.2	107.97
0.003175	108.3		108.35		108.65	108.43
dT/dx [slope]	-57.48		-66.142		-72.441	<b>-60.945</b>
dT/dx ave.	-60.945					
q" ave. (w/m^2K)	23829.495					
To ave. (degree C)	107.26					
Tw (degree C)	106.838					
T bulk (degree C)	90.900		91.000			
T bulk ave. (deg C)	90.950					
h exp. (W/m^2K)	1499.805					

<b>60</b>	0.009525	0.015875	0.022225	0.028575	0.034925	<b>Average</b>
0.022225	108.6	108.65	108.05	108	108.7	108.40
0.015875	108.6		108.85		108.9	108.78
0.009525	109.1		109.25		109.5	109.28
0.003175	109.7		109.8		110	109.83
dT/dx [slope]	-63.78		-91.34		-83.465	<b>-75.591</b>
dT/dx ave.	-75.591					



q" ave. (w/m^2K)	29556.081			
To ave. (degree C)	108.4			
Tw (degree C)	107.877			
T bulk (degree C)	90.800		91.100	
T bulk ave. (deg C)	90.950			
h exp. (W/m^2K)	1746.082			

### 30 Degrees

#### THERMOCOUPLE LOCATIONS

4	13	8	14	12
3		7		11
2		6		10
1		5		9

Y-Direction (m)	15	X-Direction (m)					Average
		0.009525	0.015875	0.022225	0.028575	0.034925	
	0.022225	91.6	91.8	91.6	91.8	91.8	
	0.015875	91.6		91.7		91.8	
	0.009525	91.6		91.7		91.85	
	0.003175	91.7		91.8		91.9	
	dT/dx [slope]	-4.72		-9.45		-5.51	<b>-4.024</b>
	dT/dx ave.	-4.024					
	q" ave. (w/m^2)	1573.384					
	To ave. (degree C)	91.72					
	Tw (degree C)	91.692					
	T bulk (degree C)	89.200			89.700		
	T bulk ave. (deg C)	89.450					
	h exp. (W/m^2K)	701.726					

20	0.009525	0.015875	0.022225	0.028575	0.034925	Average
0.022225	94.8	94.95	94.8	94.95	94.95	94.89
0.015875	94.8		94.85		94.95	94.87
0.009525	94.85		94.95		95.1	94.97
0.003175	94.95		95.1		95.15	95.07
dT/dx [slope]	-7.87		-15.75		-11.81	<b>-9.9213</b>
dT/dx ave.	-9.9213					
q" ave. (w/m^2K)	3879.2283					
To ave. (degree C)	94.89					
Tw (degree C)	94.821					

T bulk (degree C)		90.400		90.800	
T bulk ave. (deg C)	90.600				
h exp. (W/m^2K)	918.951				

25	0.009525	0.015875	0.022225	0.028575	0.034925	Average
0.022225	97	97.2	97	97.2	97.2	97.12
0.015875	97		97.1		97.2	97.10
0.009525	97.1		97.2		97.4	97.23
0.003175	97.4		97.5		97.55	97.48
dT/dx [slope]	-15.748		-20.472		-19.67	-17.375
dT/dx ave.	-17.375					
q" ave. (w/m^2K)	6793.625					
To ave. (degree C)	97.12					
Tw (degree C)	97.000					
T bulk (degree C)		90.300		90.800		
T bulk ave. (deg C)	90.550					
h exp. (W/m^2K)	1053.307					

30	0.009525	0.015875	0.022225	0.028575	0.034925	Average
0.022225	99.2	99.3	99.15	99.2	99.4	99.25
0.015875	99.2		99.2		99.4	99.27
0.009525	99.3		99.4		99.6	99.43
0.003175	99.6		99.65		99.8	99.68
dT/dx [slope]	-20.472		-26.772		-22.047	-23.097
dT/dx ave.	-23.097					
q" ave. (w/m^2K)	9030.927					
To ave. (degree C)	99.25					
Tw (degree C)	99.090					
T bulk (degree C)		90.600		90.800		
T bulk ave. (deg C)	90.700					
h exp. (W/m^2K)	1076.363					

35	0.009525	0.015875	0.022225	0.028575	0.034925	Average
0.022225	100.2	100.4	100.2	100.4	100.4	100.32
0.015875	100.2		100.3		100.4	100.30
0.009525	100.3		100.4		100.6	100.43
0.003175	100.5		100.6		100.9	100.67
dT/dx [slope]	-15.75		-20.472		-26.77	-18.478
dT/dx ave.	-18.478					
q" ave. (w/m^2K)	7224.898					
To ave. (degree C)	100.32					
Tw (degree C)	100.192					

T bulk (degree C)		90.600		90.900	
T bulk ave. (deg C)	90.750				
h exp. (W/m^2K)	765.173				

<b>40</b>	0.009525	0.015875	0.022225	0.028575	0.034925	Average
0.022225	102	102.2	101.9	102.2	102.2	102.10
0.015875	102.05		102.2		102.2	102.15
0.009525	102.1		102.2		102.6	102.30
0.003175	102.45		102.6		102.7	102.58
dT/dx [slope]	-22.05		-33.071		-29.92	<b>-25.197</b>
dT/dx ave.	-25.197					
q" ave. (w/m^2K)	9852.027					
To ave. (degree C)	102.1					
Tw (degree C)	101.926					
T bulk (degree C)		90.600		90.900		
T bulk ave. (deg C)	90.750					
h exp. (W/m^2K)	881.558					

<b>45</b>	0.009525	0.015875	0.022225	0.028575	0.034925	Average
0.022225	104.3	104.5	104.1	104.1	104.5	104.30
0.015875	104.35		104.5		104.6	104.48
0.009525	104.6		104.6		105	104.73
0.003175	104.9		105.1		105.3	105.10
dT/dx [slope]	-32.28		-44.09		-44.09	<b>-40.157</b>
dT/dx ave.	-40.157					
q" ave. (w/m^2K)	15701.387					
To ave. (degree C)	104.3					
Tw (degree C)	104.022					
T bulk (degree C)		90.600		90.800		
T bulk ave. (deg C)	90.700					
h exp. (W/m^2K)	1178.588					

<b>50</b>	0.009525	0.015875	0.022225	0.028575	0.034925	Average
0.022225	105.3	105.3	105	105	105.3	105.18
0.015875	105.4		105.5		105.5	105.47
0.009525	105.7		105.8		106	105.83
0.003175	106.1		106.3		106.5	106.30
dT/dx [slope]	-42.52		-66.142		-64.567	<b>-58.688</b>
dT/dx ave.	-58.688					
q" ave. (w/m^2K)	22947.008					
To ave. (degree C)	105.18					
Tw (degree C)	104.774					

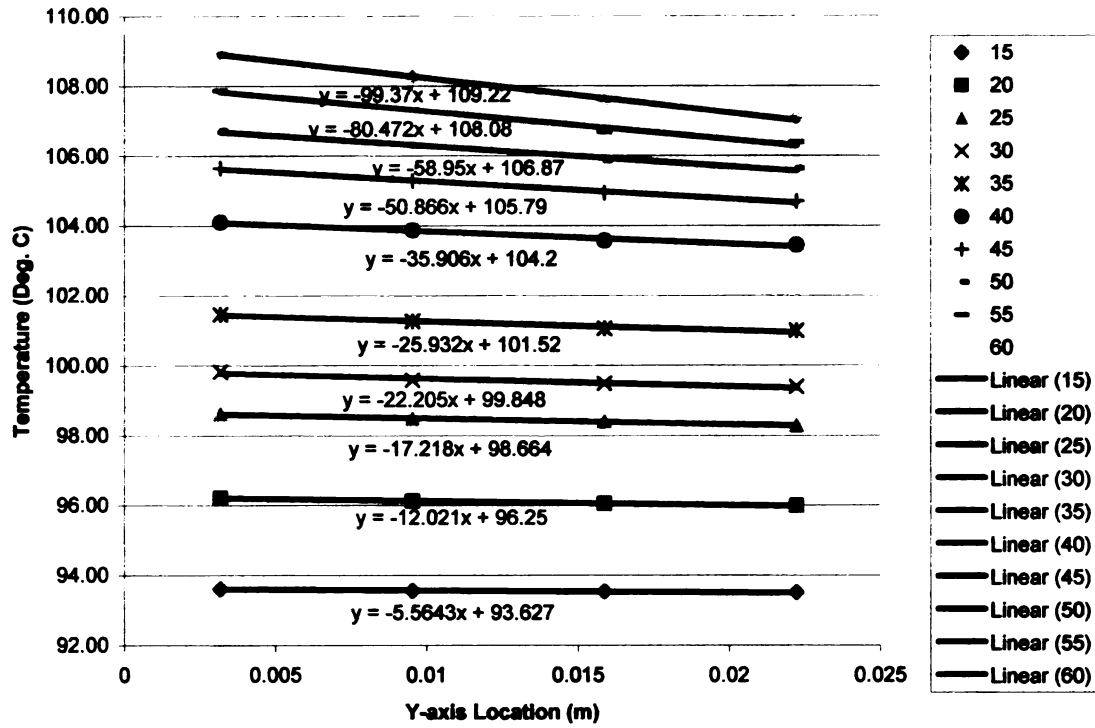
T bulk (degree C)		90.500		90.800	
T bulk ave. (deg C)	90.650				
h exp. (W/m^2K)	1624.681				

<b>55</b>	0.009525	0.015875	0.022225	0.028575	0.034925	<b>Average</b>
0.022225	106.2	106.2	105.9	105.8	106.3	106.08
0.015875	106.35		106.5		106.5	106.45
0.009525	106.7		106.9		107.2	106.93
0.003175	107.2		107.4		107.6	107.40
dT/dx [slope]	-57.48		-66.142		-72.441	<b>-70.919</b>
dT/dx ave.	-70.919					
q" ave. (w/m^2K)	27729.329					
To ave. (degree C)	106.08					
Tw (degree C)	105.589					
T bulk (degree C)		90.900		91.000		
T bulk ave. (deg C)	90.950					
h exp. (W/m^2K)	1894.157					

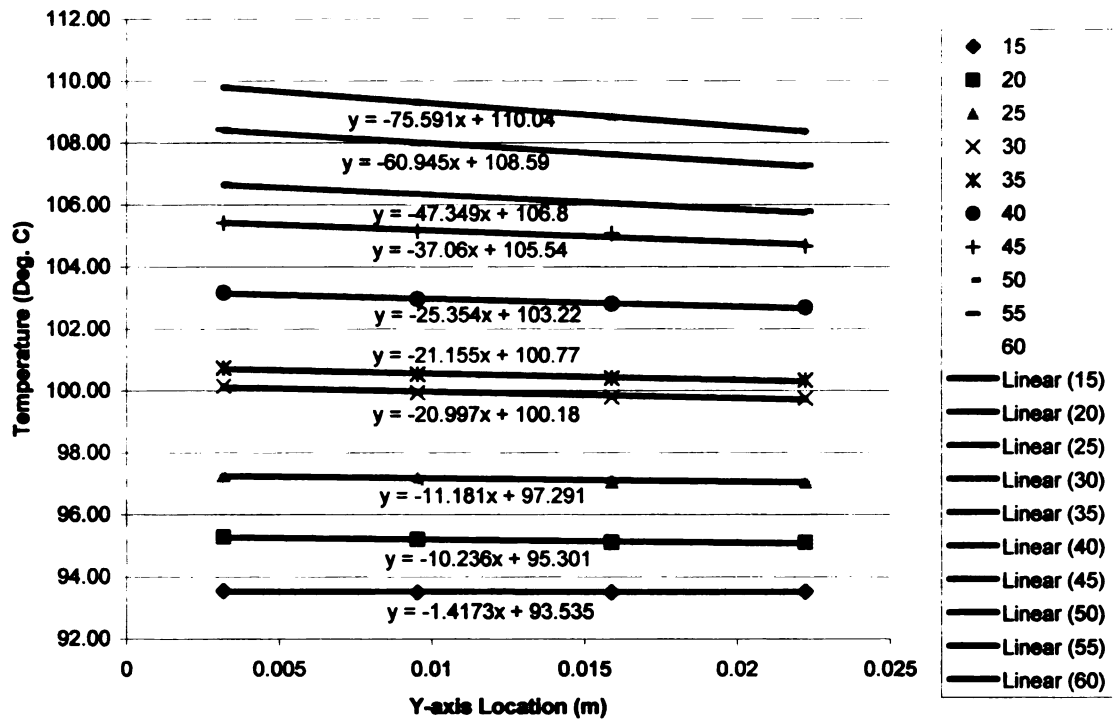
<b>60</b>	0.009525	0.015875	0.022225	0.028575	0.034925	<b>Average</b>
0.022225	107.2	107.3	106.9	107	107.5	107.18
0.015875	107.35		107.6		107.6	107.52
0.009525	107.8		108		108.4	108.07
0.003175	108.4		108.7		109	108.70
dT/dx [slope]	-63.78		-91.34		-83.465	<b>-83.937</b>
dT/dx ave.	-83.937					
q" ave. (w/m^2K)	32819.367					
To ave. (degree C)	107.18					
Tw (degree C)	106.599					
T bulk (degree C)		90.800		91.100		
T bulk ave. (deg C)	90.950					
h exp. (W/m^2K)	2097.172					

## TEMPERATURE GRADIENT PLOTS

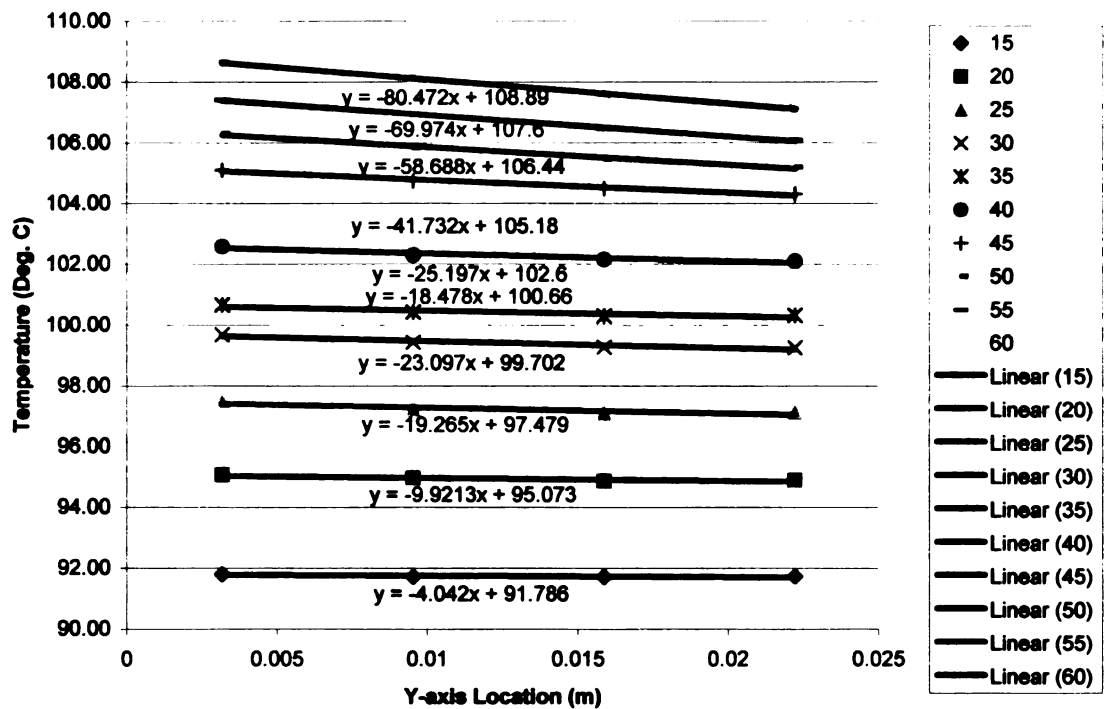
**Smooth Surface:**



### 15 Degree Surface:



### 30 Degree Surface:



## APPENDIX F

### UNCERTAINTY ANALYSIS

#### F.1 Temperature Measurement Uncertainty

Temperature was measured to the tenth of a degree, thus the uncertainty in each temperature measurement was  $0.05^{\circ}\text{C}$ . This leads to an uncertainty of  $0.2^{\circ}\text{C}$  for the measured wall superheat values.

#### F.2 Heat Flux Uncertainty

Given a  $0.05^{\circ}\text{C}$  uncertainty in each temperature measurement, the calculated heat flux values could vary by as much as 86% at low heat fluxes and only 6% at high heat fluxes.

15	X-Direction (m)					
	0.009525	0.015875	0.022225	0.028575	0.034925	
0.022225	91.6	91.8	91.6	91.8	91.8	91.75
0.015875	91.6		91.7		91.8	91.80
0.009525	91.6		91.7		91.85	91.85
0.003175	91.7		91.8		91.9	91.95
dT/dx [slope]	-4.72		-9.45		-5.51	-10.236
dT/dx ave.	-10.236					4002.28 q" uncert
q" ave. (w/m <sup>2</sup> )	4002.276					2154.41 q" exp
To ave. (degree C)	91.72					1847.87 diff
Tw (degree C)	91.649					85.7715 % diff
T bulk (degree C)		89.200		89.700		
T bulk ave. (deg C)	89.450					
h exp. (W/m <sup>2</sup> K)	1819.886					

<b>60</b>	<b>0.009525</b>	<b>0.015875</b>	<b>0.022225</b>	<b>0.028575</b>	<b>0.034925</b>		
0.022225	107.2	107.3	106.9	107	107.5	107.45	
0.015875	107.35		107.6		107.6	107.60	
0.009525	107.8		108		108.4	108.40	
0.003175	108.4		108.7		109	109.05	
dT/dx [slope]	-63.78		-91.34		-83.465	-88.189	
dT/dx ave.	-88.189					<b>34481.90</b>	<b>q" uncert</b>
q" ave. (w/m^2K)	34481.899					32634.82	<b>q" exp</b>
To ave. (degree C)	107.18					1847.08	diff
Tw (degree C)	106.570					<b>5.66</b>	<b>% diff</b>
T bulk (degree C)		90.800		91.100			
T bulk ave. (deg C)	90.950						
h exp. (W/m^2K)	2207.558						

### F.3 Solder Layer Thickness Uncertainty

The uncertainty in solder thickness between the OFHC copper blocks and test surface is assumed to be 500 microns. Variations of up to 0.6° C exist in the x-direction measured temperature of the OFHC block. A simple thermal resistance model was created to calculate these x-direction temperature values using different solder thickness values (within the uncertainty of the measurement). X-direction temperature variations of up to 0.2° C for low heat fluxes and up to 0.6° C for high heat flux were calculated. Thus variations in solder layer thickness are attributed to x-direction temperature variations.



## REFERENCES

## REFERENCES

- [1] Andrianov, A. B., V. I. Borzenko, and S. P. Malshenko. 1999. Elementary Processes at Boiling on the Surfaces with Porous Coatings. *Russ. J. Eng. Thermophys.* **9**(1-2), pp. 51-67.
- [2] Bajorek, S. M. 1988. An Experimental and Theoretical Investigation of Multicomponent Pool Boiling on Smooth and Finned Surfaces. Ph. D. Thesis, Michigan State University.
- [3] Bergles, A. E., M. C. Chyu. 1982. Characteristics of Nucleate Pool Boiling from Porous Metallic Coatings. *ASME J. Heat Transfer.* **104**, pp. 279-285.
- [4] Chang, J. Y., S. M. You. 1997. Boiling heat transfer phenomena from micro-porous and porous surfaces in saturated FC-72. *Int. J. Heat Mass Transfer.* **40**(18), pp. 4437-4447.
- [5] Chang, J. Y., S. M. You. 1997. Enhanced boiling heat transfer from micro-porous surfaces: effects of coating composition and method. *Int. J. Heat Mass Transfer.* **40**(18), pp. 4449-4460.
- [6] Chien, L., R. L. Webb. 1998. A Parametric Study of Nucleate Boiling on Structured Surfaces, Part I: Effect of Tunnel Dimensions. *ASME J. Heat Transfer.* **120**, pp. 1042-1048.
- [7] Chien, L., R. L. Webb. 1998. A Parametric Study of Nucleate Boiling on Structured Surfaces, Part II: Effect of Pore Diameter and Pore Pitch. *ASME J. Heat Transfer.* **120**, pp. 1049-1054.
- [8] Chien, L., R. L. Webb. 1998. Measurement of bubble dynamics on an enhanced boiling surface. *Experimental Thermal and Fluid Science.* **16**, pp. 177-186.
- [9] Chien, L., R. L. Webb. 2001. Effect of Geometry and Fluid Property Parameters on Performance of Tunnel and Pore Enhanced Boiling Surfaces. *Enhanced Heat Transfer.* **8**, pp. 329-339.
- [10] Clark, H. B., P. S. Strengewater, and J. W. Westwater. 1959. Active sites for nucleate boiling. *Chem. Eng. Prog. Symp. Ser.* **55**(29), pp. 103-110.
- [11] Honda, H., H. Takamatsu, and J. J. Wei. 2002. Enhanced Boiling of FC-72 on Silicon Chips with Micro-Pin-Fins and Submicron-Scale Roughness. *ASME J. Heat Transfer.* **124**, pp. 383-390.
- [12] Hong, K. T., H. Imadojemu, R. L. Webb. 1994. Effects of contact angle and surface roughness on contact angle. *Experimental Thermal and Fluid Science.* **8**, pp. 279-285.

- [13] Hsieh S., P. Hsu. 1994. Nucleate boiling characteristics of R-114, distilled water, and R-134a on plain and rib-roughened tube geometries. *Int. J. Heat Mass Transfer*. **37**(10), pp. 1423-1432.
- [14] Hsieh, S. T. Yang. 2001. Nucleate pool boiling from coated and spirally wrapped tubes in saturated R-134a and R-600 at low and moderate heat flux. *ASME J. Heat Transfer*. **123**, pp. 257-270.
- [15] Hsieh, S., C. Ke. 2002. Bubble Dynamics Parameters and Pool Boiling Heat Transfer on Plasma Coated Tubes in Saturated R-134a and R-600a. *ASME J. Heat Transfer*. **124**, pp. 704-716.
- [16] Kedzierski, M. A., J. L. Worthington. 1993. Design and Machining of Copper Specimens with Micro Holes for Accurate Heat Transfer Measurements. *Experimental Heat Transfer*. **6**, pp. 329-344.
- [17] Kedzierski, M. A. 1995. Calorimetric and Visual Measurements of R123 Pool Boiling on Four Enhanced Surfaces. NISTIR 5732. U.S. Department of Energy, Washington, DC.
- [18] Kim, J. H., K. N. Rainey, S. M. You, and J. Y. Pak. 2002. Mechanism of Nucleate Boiling Heat Transfer Enhancement From Microporous Surfaces in Saturated FC-72. *ASME J. Heat Transfer*. **124**, pp. 500-506.
- [19] Kovalev, S. A., V. Lenykov, N. Afgan, and L. Jovic. 1985. Boiling heat transfer from surfaces with porous layers. *Int. J. Heat Mass Transfer*. **28**(2), pp. 415-422.
- [20] Leontiev, A. I., J. R. Lloyd, S. P. Malysenko, V. I. Borzenko, D. O. Dunikov, A. A. Eronin, and O. V. Nazarova. 2003. New effects in interfacial heat and mass transfer of boiling and evaporation in micro-scale porous materials. Accepted for presentation at the 2003 ASME IMECE, Washington D.C., November 2003.
- [21] Lloyd, J. 1971. Laminar, Transition, and Turbulent Natural Convection Adjacent to Vertical and Upward-Facing Inclined Surfaces. Ph. D. Thesis, University of Minnesota.
- [22] Lloyd, J. R., E. M. Sparrow, and E. R.G. Eckert. 1972. Laminar transition and natural convection adjacent to inclined and vertical surfaces. *Int. J. Heat Mass Transfer*. **15**(3), pp. 457-473.
- [23] Lloyd, J. R., E. M. Sparrow, and E. R.G. Eckert. 1972. Local natural convection mass transfer measurements. *J. Electrochemical Society*. **119**(6), pp. 702-707.
- [24] Mertz., R., M. Groll, L. L. Vasiliev, and V. V. Khrolenok. 1998. 11<sup>th</sup> International Heat Transfer Conference. Kyongju, Korea.

- [25] Moran, W. R. 1974. Free Convection and Mass Transfer Adjacent to Vertical and Downward-Facing Inclined Surfaces. Masters Thesis, Notre Dame, Indiana.
- [26] Nishikawa, K., T. Ito, and K. Tanaka. 1979. Enhanced heat transfer by nucleate boiling at sintered metal layer. *Heat Transfer Jap. Res.* **8**(2), pp 65-81.
- [27] Ramaswamy, C., Y. Joshi, W. Nakayama, W. B. Johnson. 2003. Effects of Varying Geometrical Parameters on Boiling from Microfabricated Enhanced Structures. *ASME J. Heat Transfer.* **125**, pp. 103-109.
- [28] Rainey, K. N., S. M. You. 2000. Pool Boiling Heat Transfer from Plain and Microporous, Square Pin-Finned Surfaces in Saturated FC-72. *ASME J. Heat Transfer.* **122**, pp. 509-516.
- [29] Rainey, K. N., S. M. You, and S. Lee. 2003. Effect of Pressure, Subcooling, and Dissolved Gas on Pool Boiling Heat Transfer from Microporous Surfaces in FC-72. *ASME J. Heat Transfer.* **125**, pp. 75-83.
- [30] Shakir, S. 1987. Boiling Incipience and Heat Transfer on Smooth and Enhanced Surfaces. Ph. D. Thesis, Michigan State University.
- [31] Snyder, T. J., J. N. Chung, and J. B. Schneider. 1998. Competing Effects of Dielectrophoresis and Buoyancy on Nucleate Boiling and a Analogy with Variable Gravity Boiling Results. *ASME J. Heat Transfer.* **120**, pp. 371-379.
- [32] Thome, J. R. 1990. Enhanced Boiling Heat Transfer. Hemisphere Publishing Corp.
- [33] Webb, R. L. 1983. Nucleate Boiling on Porous Coated Surfaces. *Heat Transfer Engineering.* **4**(2-3), pp. 71-82.
- [34] You, S. M., T. W. Simon, A. Bar-Cohen, and W. Tong. 1990. Experimental investigation of nucleate boiling incipience with a highly-wetting dielectric fluid (R-113). *Int. J. Heat Mass Transfer.* **33**(1), pp. 105-117.

MICHIGAN STATE UNIVERSITY



3 1293 02504